

1 **This article is a preprint published at EarthArXiv**

2 **Notice - From the AMS Copyright Policy section 7c:**

3 This work has been submitted to the Journal of Climate. Copyright in this work may be
4 transferred without further notice. This work has not yet been peer-reviewed and is pro-
5 vided by the contributing author(s) as a means to ensure timely dissemination of schol-
6 arly and technical work on a noncommercial basis. Copyright and all rights therein are
7 maintained by the author(s) or by other copyright owners. It is understood that all per-
8 sons copying this information will adhere to the terms and constraints invoked by each au-
9 thor's copyright. This work may not be reposted without explicit permission of the copy-
10 right owner. [https://www.ametsoc.org/index.cfm/ams/publications/ethicalguidelines- and-ams-](https://www.ametsoc.org/index.cfm/ams/publications/ethicalguidelines-and-ams-policies/ams-copyright-policy)
11 [policies/ams-copyright-policy.](https://www.ametsoc.org/index.cfm/ams/publications/ethicalguidelines-and-ams-policies/ams-copyright-policy)

12 **Feedbacks on zonal mean tropical precipitation shifts induced by land**
13 **surface change**

14 Marysa M. Laguë*

15 *Department of Earth and Planetary Science, University of California, Berkeley, Berkeley, CA,*
16 *USA*

17 Abigail L. S. Swann

18 *Department of Atmospheric Sciences, University of Washington, Seattle, WA, USA*

19 *Department of Biology, University of Washington, Seattle, WA, USA*

20

William R. Boos

21

Department of Earth and Planetary Science, University of California, Berkeley, Berkeley, CA,

22

USA

23

Climate and Ecosystem Sciences Division, Lawrence Berkeley National Laboratory, Berkeley,

24

CA, USA

25

**Corresponding author address: Marysa M. Laguë, Department of Earth and Planetary Science,*

26

University of California Berkeley, 307 McCone Hall, Berkeley, CA 94720.

27

E-mail: mlague@berkeley.edu

ABSTRACT

28 Changes in land surface albedo and land surface evaporation modulate the
29 atmospheric energy budget by changing temperatures, water vapor, clouds,
30 snow and ice cover, and the partitioning of surface energy fluxes. Here ide-
31 alized perturbations to land surface properties are imposed in a global model
32 to understand how such forcings drive shifts in zonal mean atmospheric en-
33 ergy transport and zonal mean tropical precipitation. For a uniform decrease
34 in global land albedo, the albedo forcing and a positive water vapour feed-
35 back contribute roughly equally to increased energy absorption at the top of
36 the atmosphere (TOA), while radiative changes due to the temperature and
37 cloud cover response provide a negative feedback and energy loss at TOA.
38 Decreasing land albedo causes a northwards shift in the zonal mean intertrop-
39 ical convergence zone (ITCZ). The combined effects on ITCZ location of all
40 atmospheric feedbacks roughly cancel for the albedo forcing; the total ITCZ
41 shift is comparable to that predicted for the albedo forcing alone. For an im-
42 posed increase in evaporative resistance that reduces land evaporation, low
43 cloud cover decreases in the northern mid-latitudes and more energy is ab-
44 sorbed at TOA there; longwave loss due to warming provides a negative feed-
45 back on the TOA energy balance and ITCZ shift. Imposed changes in land
46 albedo and evaporative resistance modulate fundamentally different aspects
47 of the surface energy budget. However, the pattern of TOA radiation changes
48 due to the water vapour and air temperature responses are highly correlated
49 for these two forcings because both forcings lead to near-surface warming.

50 **1. Introduction**

51 Changes in land surface properties, such as those associated with changes in vegetation, modu-
52 late fluxes of energy and water between land and the overlying atmosphere (??????). Changes in
53 land surface properties can directly modify surface temperatures by re-partitioning surface energy
54 fluxes between sensible and latent components (???). By modifying the overlying atmosphere,
55 land surface changes can also indirectly alter local surface climate by changing radiation and sur-
56 face turbulent fluxes in ways that constitute feedbacks on the original land surface perturbation (?).
57 Furthermore, land-driven atmospheric changes can lead to changes in terrestrial climate both in
58 the region of the original land surface change and in regions far removed from that initial change
59 (??????).

60 Changes in land surface properties modify climate by modulating the flux of energy between
61 land and the base of the atmosphere. Surface albedo directly influences the solar energy absorbed
62 by land, with darker land such as forests absorbing more sunlight than brighter land such as deserts
63 (????, and references therein). The land surface has a small heat capacity compared to the ocean
64 and does not efficiently move energy laterally (????). Thus, over annual timescales, changes in
65 solar and longwave energy absorbed by land cause changes in longwave radiation, sensible heat,
66 and latent heat emitted by land; that is, the land surface energy budget is closed over sufficiently
67 long timescales such as the annual cycle (??). Latent heat flux from land to the atmosphere is
68 modulated not only by surface water availability and atmospheric water vapor demand, but also by
69 physical properties of the land surface (??). For example, vegetation can actively modify the flux
70 of water from land to the atmosphere by regulating transpiration through the opening and closing
71 of stomata (leaf pores that control gas exchange) (?).

72 Changes in land surface albedo and evaporation have been demonstrated to be capable of driving
73 large-scale shifts in atmospheric circulation (??). ? explored the effects of albedo, evaporation,
74 and roughness of a completely forested vs. grass-covered world, while ? demonstrated how mid-
75 latitude forest cover can shift the location of the Intertropical Convergence Zone (ITCZ) in a global
76 climate model. Such changes in global circulation can be understood, in part, using the vertically
77 integrated atmospheric energy budget. For example, changes in surface ice cover, vegetation,
78 or idealized energy sources have been shown to modify large-scale atmospheric circulation and
79 tropical precipitation, with the zonal mean location of the ITCZ shifting towards the energy-rich
80 hemisphere (??) or, more precisely, toward the hemisphere containing the anomalous positive
81 energy source (??????).

82 To understand the atmospheric response to an imposed change in the climate system, it can
83 be useful to decompose the response into that produced directly by the forcing and that arising
84 from individual feedbacks. For example, increased atmospheric carbon dioxide concentrations
85 directly affect longwave radiation (the forcing) and initiate feedbacks by other aspects of the cli-
86 mate system (e.g. changes in cloud cover or sea ice extent) which further modify shortwave (SW)
87 and longwave (LW) radiation at both the top of the atmosphere (TOA) and the surface (?). For
88 low-latitude rainfall changes, these feedbacks can be large compared to the forcing (??), mak-
89 ing it difficult to understand and predict how an imposed land surface change which modifies the
90 atmospheric energy budget will alter local and remote surface climate.

91 In this study, we investigate how idealized changes in land surface properties modify large-
92 scale atmospheric circulation and precipitation, both through their direct effect on fluxes of energy
93 into the atmosphere and through radiative feedbacks. We first use climate model simulations
94 to study how global-scale changes in land surface albedo and evaporative resistance modify the
95 atmospheric energy source (i.e. the net flux of energy into the atmosphere through its top and

96 bottom boundaries). While many more studies have focused on the influence of land surface
97 albedo on climate (e.g. ???), evaporative resistance is also important (e.g. ???). Evaporative
98 resistance controls the surface latent heat flux for a given vapor pressure deficit of surface air, and
99 is a bulk proxy for many surface and vegetative processes that control water vapor flux.

100 We attribute changes in the atmospheric energy source to the direct effect of the imposed land
101 surface change (in albedo or evaporative resistance) and to feedbacks resulting from (i) albedo
102 changes due to snow and ice cover, (ii) changes in atmospheric water vapour, (iii) changes in
103 temperatures, and (iv) changes in cloud cover. Each of these components of the change in the
104 atmospheric energy source can, through the vertically integrated atmospheric energy budget, be
105 directly associated with a change in atmospheric energy transport. Since, in Earth's tropics, both
106 precipitation and atmospheric energy transport are primarily accomplished by time-mean overturn-
107 ing circulations, this allows us to attribute changes in tropical circulation and tropical precipitation
108 to the imposed land surface forcing and the feedbacks.

109 **2. Methods**

110 *a. Model*

111 We use a modified version of the Community Earth System Model (CESM) (?), consisting of the
112 Community Atmosphere Model v. 5 (CAM5) coupled to a slab ocean model, the CICE5 interactive
113 sea ice model (?), and a simplified land model. The slab ocean allows sea surface temperatures
114 (SSTs) to change but uses prescribed ocean heat transport (?); this allows atmospheric circulation
115 more freedom to change over both land and oceans than in a fixed-SST simulation. The prescribed
116 ocean heat transport is identical across all simulations. Instead of the Community Land Model
117 (CLM) (??), we use the Simple Land Interface Model (SLIM) (?), which allows us to explicitly

118 control individual land surface properties in a way that is not possible with more complex land
119 surface models such as CLM. Simulations are run at roughly 2° horizontal resolution.

120 *b. Simulations*

121 Two land surface properties are perturbed for this study: albedo and evaporative resistance.
122 Albedo is a measure of the fraction of incident shortwave radiation that the land surface reflects,
123 while evaporative resistance modifies the difficulty of evaporating water from land. In the context
124 of vegetation, albedo is modulated by leaf color, leaf angle, and leaf area; evaporative resistance
125 is a combined result of soil moisture, root depth, leaf area, and stomatal conductance. In SLIM,
126 both surface properties are directly controlled by the user.

127 We modify the prescribed, snow-free albedo of the land surface for visible shortwave radiation
128 (both direct and diffuse streams). A portion of the total modelled shortwave radiation incident
129 upon the land surface occurs in the near-infrared (near-IR), but we hold the snow-free land surface
130 albedo in the near-IR fixed across all simulations. We only modify the land surface albedo over
131 non-glaciated regions. The total land surface albedo can be modified by the presence of snow,
132 which masks the bare-ground albedo and results in a brighter surface; as such, the actual change
133 in albedo that affects radiation is smaller than the snow-free albedo change imposed on the land
134 surface.

135 The evaporative resistance that we modify in SLIM modulates the difficulty of evaporating water
136 from land. The hydrology in SLIM is represented by a bucket at each land point. To evaporate
137 water from the bucket, there is a combined resistance due in part to how full the bucket is (analo-
138 gous to soil moisture), and in part to the imposed evaporative resistance at each point (analogous
139 to properties such as vegetation root depth or stomatal conductance). It is this second resistance
140 term which we modify in our simulations; the soil moisture is free to evolve.

141 Three primary simulations are used in this study, while two additional simulations are leveraged
142 to calculate the relationship between ITCZ latitude and cross-equatorial atmospheric energy trans-
143 port. Each simulation is run for a total of 50 years, with the first 20 years discarded to allow the
144 model time to spin up. Note that the model simulations used in this study are a subset of the same
145 simulations used in ?.

146 The first “baseline” simulation uses moderate values for land surface albedo ($\alpha = 0.2$) and
147 evaporative resistance ($r_s = 100$ s/m). The second simulation explores the effect of making land
148 darker ($\alpha = 0.1$, $r_s = 100$ s/m), while the third explores the effect of making it harder to evaporate
149 water from land ($\alpha = 0.2$, $r_s = 200$ s/m). An albedo of 0.2 is roughly comparable to that of a
150 grassland, while an albedo of 0.1 is comparable to that of a forest (see ?, and references therein). A
151 change in evaporative resistance from 200 to 100 s/m is comparable to a change in the canopy-level
152 stomatal conductance between needleleaf and broadleaf forests (?). Two additional simulations
153 from ?—one with a land surface albedo of 0.3, which is comparable to that of a desert, and the
154 other with an evaporative resistance of 30 s/m, which is comparable to that of a well-watered
155 crop—are used to calculate the relationship between annual mean cross-equatorial atmospheric
156 energy transport AET_{eq} and annual mean ITCZ latitude as measured by the center of mass of
157 tropical precipitation, ϕ_p (see appendix for calculations of AET_{eq} and ϕ_p). These simulations each
158 provide an additional 30 years of spun-up data for our linear fit of ΔAET_{eq} vs. $\Delta \phi_p$.

159 All other land surface properties are identical across simulations, and across space. That is,
160 all simulations have the same spatially uniform values for aerodynamic roughness (0.1 m), the
161 capacity of land to hold water (200 mm), soil thermal properties, etc. Glaciated land points have
162 thermal and radiative properties consistent with ice (?).

163 *c. Approach*

164 Here, we outline the general approach used in this study. Details on specific calculations are
165 provided in the Appendix. We modify each of the two land surface properties (albedo and evap-
166 orative resistance) in isolation. Each change in land surface property drives a change in net TOA
167 radiation (TOA_{net}), a change in zonal mean cross-equatorial atmospheric heat transport, and a shift
168 in the zonal mean location of the ITCZ.

169 Using a combination of model output and radiative kernels for albedo, temperature, and water
170 vapour, we decompose the total change in TOA radiation into the change in TOA *SW* directly due
171 to the imposed change in land surface albedo, the change in TOA *SW* due to changes in albedo
172 from changes in snow/ice cover, the change in TOA *LW* due to changes in surface temperature
173 and atmospheric temperatures, the changes in TOA *SW* and *LW* due to changes in column water
174 vapour, and the changes in TOA *SW* and *LW* due to changes in cloud cover.

175 We meridionally integrate TOA_{net} , under the assumption that atmospheric energy storage is
176 negligible on annual time scales, to calculate cross-equatorial atmospheric energy transport AET_{eq} ,
177 and estimate the linear relationship between AET_{eq} and the zonal-mean location of the ITCZ.
178 We measure the zonal-mean ITCZ location as the latitude ϕ_p that is the center of mass of the
179 precipitation distribution between 20°S-20°N. Using the individual contribution to ΔTOA_{net} from
180 each surface or atmospheric process resulting from the imposed change in land surface property
181 (e.g. the change in albedo from changes in snow/ice, or the change in water vapour), we determine
182 the ΔAET_{eq} that would result from that individual component of the TOA_{net} response alone. We
183 then leverage the derived relationship between AET_{eq} and ϕ_p to attribute portions of the total
184 modelled shift in the ITCZ to each individual atmospheric and surface process. The practice of

185 meridionally integrating anomalous TOA energy sources to obtain an AET_{eq} change and then an
186 ITCZ shift follows ?, and using this procedure to estimate radiative feedbacks follows ?.

187 We follow the methodology of ? and ? to decompose the response of TOA radiation into
188 components associated with changes in imposed land surface albedo, changes in albedo due to
189 changes in snow and ice, changes in water vapor, changes in surface and air temperatures, and
190 changes in cloud cover. Details of the calculations used in this study are provided in the Appendix.

191 3. Results

192 Decreasing land surface albedo and increasing land surface evaporative resistance both gener-
193 ate changes in the TOA energy balance with distinct spatial and seasonal patterns (figure ??).
194 Decreasing land surface albedo results in more energy absorbed at the TOA over most land re-
195 gions, particularly during local summer when insolation is high, while increasing land surface
196 evaporative resistance modifies the TOA energy budget mostly in the northern mid-to-high lati-
197 tudes during boreal summer. Decreasing land albedo and increasing land evaporative resistance
198 both lead to overall more energy absorbed at the TOA over the Northern Hemisphere, though for
199 different reasons which are explored below.

200 The land albedo and evaporative resistance changes also produce changes in precipitation over
201 both land and ocean throughout the globe. Past studies have demonstrated that hemispheric im-
202 balances in atmospheric energy sources lead to shifts in the ITCZ towards the positive energy
203 source anomaly (e.g. ??????). In our simulations, changes in land surface albedo and evaporative
204 resistance both lead to northward shifts in the ITCZ (figure ??; the general pattern of positive
205 precipitation anomalies to the north of the equator and negative anomalies to the south indicate a
206 northward shift of the tropical precipitation maximum). Here, we investigate the mechanisms con-
207 tributing to the change in the TOA energy budget, and quantify the association between changes

208 in the TOA radiative balance and changes in the atmospheric energy transport and zonal mean
209 tropical precipitation. We focus these analyses on the annual mean.

210 *a. Decreasing Land Surface Albedo*

211 The spatially uniform decrease in snow-free land albedo has a spatially non-uniform impact on
212 TOA_{net} . Darkening land results in more *SW* being absorbed by Earth over most land areas, while
213 over oceans and parts of the northern high-latitudes, more energy is lost by the Earth system (figure
214 ??a). The peak anomalous energy gain resulting from the decreased land albedo is found in the
215 tropics in the annual mean, with smaller increases in the mid-latitudes.

216 To understand the mechanisms through which a spatially uniform change in land surface albedo
217 causes a spatially non-homogeneous and non-local change in TOA radiation, we decompose the
218 response into a forcing and several feedbacks, each of which impact the TOA flux of shortwave
219 (*SW*) or longwave (*LW*) radiation. For our analysis of changes in TOA energy fluxes, all fluxes
220 (*SW* and *LW*) are defined to be positive *downwards* such that positive anomalies indicate more
221 energy into the Earth system.

222 1) ALBEDO FORCING

223 The imposed decrease in land surface albedo directly forces an increase in absorbed solar ra-
224 diation at the surface, and in turn reduces the amount of *SW* leaving the atmosphere at the TOA.
225 Using the all-sky (i.e. including the effects of clouds) radiative kernel for albedo for CAM5 (?),
226 we calculate how our imposed change in land surface albedo directly modifies TOA *SW* assuming
227 temperatures, water vapour, snow and ice cover, and cloud cover do not change. The imposed
228 decrease in land surface albedo causes an increase in net TOA *SW* radiation over all non-glaciated
229 land areas (that is, everywhere the albedo was directly changed; figure ??a). Within snow-free

230 land regions, the spatial pattern in the change in TOA *SW* radiation comes predominantly from
231 the spatial pattern of the radiative kernel itself, which reflects the pattern of insolation, cloudiness,
232 and clear-sky optical depth (figure S1). From the kernel, we see that the increase in absorbed TOA
233 *SW* for a spatially uniform decrease in land albedo is largest in low latitudes, where incident solar
234 radiation is highest and the annual mean atmospheric path length for downwelling shortwave is
235 smallest. The same albedo change imposed on regions with climatologically high cloud cover (e.g.
236 the Maritime Continent) has a smaller impact on TOA *SW* than regions at a similar latitude with
237 less cloud cover, as less *SW* reaches the surface in those regions. The direct forcing of the imposed
238 albedo change is calculated here specifically for snow-free albedo, i.e. how the TOA *SW* would
239 be affected in the absence of snow. However, land surface albedo in higher latitudes is masked
240 by snow for part of the year; the change in TOA radiation because of changes in snow and ice is
241 captured in the albedo feedback term discussed next.

242 2) ALBEDO FEEDBACK

243 We define albedo feedbacks as changes in TOA *SW* radiation due to changes in snow and ice
244 cover, which themselves result from changes to the climate system *driven* by our imposed change
245 in land surface property. Decreasing land surface albedo leads to warming near the land surface
246 (see ?), causing sea ice loss and changes in snow cover in the high latitudes (supplemental figures
247 S2, S3). Using the radiative kernel for albedo, we can quantify the effect of albedo changes
248 resulting from changes in snow and ice on TOA *SW*. The albedo feedback on the imposed decrease
249 in snow-free land albedo is positive (i.e. more *SW* absorbed at the TOA) over regions of snow and
250 sea ice loss, with most of the changes occurring in the northern high latitudes (with some loss of
251 sea ice along the ice edge of Antarctica; figure ??b).

252 3) WATER VAPOUR FEEDBACKS

253 Decreased land surface albedo can modify atmospheric water vapour both by modulating evapo-
254 ration from the land surface and by modulating the winds that transport water vapour. Decreasing
255 land albedo leads to more water vapour over tropical land in our model, with atmospheric tem-
256 peratures and specific humidities both generally increasing over land. There is also a meridional
257 dipole pattern in precipitable water over tropical oceans reflecting a northwards shift in the ITCZ
258 and a change in the humidity of the subtropical dry zones (figure S4). In idealized aquaplanet
259 models, the relative humidity of the subtropical dry zones increases in the hemisphere in which
260 a positive energy source is imposed and decreases in the subtropical dry zones on the other side
261 of the equator, amplifying the more traditional fixed-relative humidity water vapor feedback (?);
262 this also seems to occur in our model in response to land albedo changes. The only statistically
263 significant changes in *SW* at the TOA due to water vapour changes in response to decrease land
264 albedo occur over the Sahara and Arabian Peninsula, where the response is positive (i.e. more *SW*
265 absorbed by the enhanced water content; figure ??c). The *LW* effects of water vapour changes are
266 also positive, but are much more far reaching, spreading over most land and ocean regions of the
267 NH (figure ??d). Averaged globally, the *LW* effects of changes in atmospheric water vapour are
268 as large as the direct effect of both the albedo forcing and ice-albedo feedback on TOA *SW*, with
269 both contributing an extra 2 W/m^2 of energy to the Earth system at the TOA (table ??).

270 4) TEMPERATURE FEEDBACKS

271 Temperature feedbacks are changes in TOA *LW* due to changes in surface temperature, T_s , and
272 temperatures through the atmospheric column. These combine the Planck and lapse rate feed-
273 backs, with the latter typically having a magnitude that is about one-third that of the former in the
274 global mean (?). Using the radiative kernel for temperature, we see that temperature feedbacks

275 produce an increase in outgoing *LW* that opposes the *SW* forcing, as expected for negative feed-
276 backs. Changes in T_s drive an increase in outgoing *LW* mostly over NH land and the Arctic ocean
277 (figure S5). In contrast, changes in atmospheric temperatures result in more outgoing *LW* over
278 most land and ocean regions, due to large-scale atmospheric warming as a result of decreasing
279 land albedo (figure ??e). Changes in TOA *LW* in response to decreased land albedo provide the
280 strongest globally averaged change in the TOA energy budget, yielding a global average of 2.8
281 W/m^2 of energy loss at the TOA (table ??). This is expected for the negative Planck and lapse rate
282 feedbacks, which balance the sum of the forcing and the positive water vapor and albedo feedbacks
283 to achieve TOA energy balance in the new steady state.

284 5) CLOUD FEEDBACKS

285 Cloud feedbacks are changes to net TOA *SW* and *LW* as a result of changes in cloud cover.
286 Changes in cloud radiative forcing that occur in the absence of any changes in cloud cover are
287 not included in this definition of cloud feedbacks, as detailed in the Appendix and discussed by
288 ?. We consider cloud feedbacks to be positive if the change in cloud cover leads to an increase in
289 net energy absorbed at the TOA. Globally, the combined *SW* and *LW* effect of changes in cloud
290 cover in response to decrease land albedo is a net loss of energy from the Earth system (figure
291 ??f). Over most land regions, a decrease in land albedo results in an increase in cloud cover that
292 accompanies the precipitation increase (e.g. figure ??a), producing greater reflection of TOA *SW*
293 (figure ??g) and enhanced *LW* trapping over land (figure ??h). Some reductions in cloud cover
294 occur over ocean, with reduced *SW* reflection and reduced *LW* trapping by clouds being especially
295 prominent where reduced rainfall south of the equator accompanies the northward shift of the
296 ITCZ (cf. figures ??a and ??g, h). The *SW* and *LW* effects of cloud changes nearly cancel in
297 regions where high cloud changes accompany ITCZ shifts, while the *SW* effects of cloud changes

298 dominate in regions where low clouds change (e.g. the upwelling zones in eastern ocean basins).
299 However, in the global mean the effects of cloud changes are negative in both the LW and SW ,
300 which contribute roughly equally to the global mean cloud feedback (table 1).

301 *b. Increasing Land Surface Evaporative Resistance*

302 Unlike decreasing land albedo, which causes more SW energy to be absorbed by land, chang-
303 ing the evaporative resistance of land does not directly modify the total energy absorbed by land.
304 Increasing evaporative resistance drives a repartitioning of surface energy fluxes, where energy
305 previously used to evaporate water is instead partitioned into sensible heat flux or emitted long-
306 wave radiation, both of which result from the increase in surface temperature that is driven by the
307 reduced evaporative cooling. Changes in evaporative resistance can only modify latent heat flux
308 from the surface to the atmosphere in regions where there is water stored on the land surface; there
309 is little to no effect of changing this surface property over desert regions.

310 Here we discuss the net response to the evaporative resistance forcing, and briefly summarize all
311 of the individual components of that response. In contrast to the response of TOA_{net} to decreasing
312 land albedo, increasing the evaporative resistance of land results in an increase in TOA_{net} that
313 is strongest in the northern mid-latitudes during June-August (figure ??b, d). As stated above,
314 changing the evaporative resistance of land has no *direct* impact on the total energy absorbed by
315 land, so there is no “forcing” in the context used for the albedo simulations. However, we can still
316 decompose changes in the TOA energy budget into components due to snow/ice changes, water
317 vapour, temperatures, and clouds.

318 Increasing the evaporative resistance of land leads to warming by suppressing latent cooling of
319 the land surface, which causes a reduction of snow and sea-ice (figure S3). This reduces the surface
320 albedo and leads to an increase in absorbed SW at the TOA, mostly in the northern high latitudes

321 during boreal summer (figure ??d, ??b; note the change in color scale in figure ??). There are no
322 statistically significant changes in TOA *SW* due to changes in atmospheric water vapour, while the
323 *LW* effects of water vapour changes lead to a slight increase in energy absorbed by Earth at the
324 TOA over parts of the low latitude ocean (figure ??c, d). We note that total column water vapor
325 actually increases over most of the Northern Hemisphere, which has the largest land area (figure
326 4b). That is, increased land resistance leads to decreased land evaporation and less low cloud
327 cover, which drives warming which itself results in more atmospheric water vapor, particularly
328 over the oceans, resulting from suppressed terrestrial evaporation. Increased surface temperatures
329 in the Arctic lead to more TOA *LW* loss, while atmospheric warming in the northern mid- to
330 high-latitudes also increases TOA *LW* loss (figure ??e).

331 The largest change to TOA radiation as a result of increasing the evaporative resistance of land
332 comes from the *SW* effects of changes in cloud cover (figure ??f,g). Loss of cloud cover over
333 southeastern North America and western Eurasia results in an increase in *SW* absorption by Earth.
334 This signal is strongest during NH summer, but persists with weaker magnitude over southeast-
335 ern North America during NH winter (figure ??d,f). Averaged globally, the *SW* and *LW* effects
336 of cloud cover changes on TOA_{net} , resulting from increased land surface evaporative resistance,
337 largely cancel (table ??).

338 *c. Cloud Forcing vs. Feedback*

339 In the previous two sections we quantified the cloud feedback, which results from a change in
340 cloud cover and is distinct from a change in the net radiative effects of clouds (which, in turn, is
341 often referred to as the cloud forcing; ?). This distinction is important for our imposed change
342 in land surface albedo because the surface albedo change modifies the effect of a fixed cloud
343 distribution on the TOA *SW* flux, thus driving a change in *SW* cloud forcing independent of any

344 change in cloud cover. That is, changes in *SW* cloud forcing (figure S6). occur both because
345 of changes in cloud cover (the *SW* cloud feedback described above) and because of changes in
346 surface *SW* fluxes driven by the change in albedo independent of any changes in cloud cover. The
347 global mean *SW* cloud forcing is more than twice as large as the global mean cloud feedback for
348 the albedo forcing (-1.2 W/m² vs -0.5 W/m²). However, the *SW* cloud forcing and *SW* cloud
349 feedback are very similar for an increase in land evaporative resistance, because in that case nearly
350 all of the change in *SW* cloud forcing comes directly from a change in cloud cover. The same
351 physical process is thus captured by the *SW* cloud feedback and *SW* cloud forcing for changes in
352 evaporative resistance (figure S7).

353 *d. Pattern Correlation*

354 The pattern of the total TOA radiative response to a change in albedo or evaporative resistance
355 differs substantially (compare figure ?? a/b), with the two having a pattern correlation coefficient
356 of only 0.3 (table ??). However, for particular components of the TOA energy budget decompo-
357 sition explored above, the pattern is very similar for both forcings. Despite the two land surface
358 properties modifying fundamentally different aspects of the surface energy budget, the pattern of
359 the TOA response due to changes in water vapour, surface temperature, and air temperature are
360 similar for changes in albedo and evaporative resistance (compare individual panels of figure ??
361 to those in ??). Indeed, the pattern of the TOA response due to changes in water vapour, sur-
362 face temperature, and air temperature are strongly correlated for a change in land surface albedo
363 and land surface evaporative resistance (pattern correlation coefficients range from 0.7 to 0.9; table
364 ??). This is because both the water vapour and temperature components of the TOA energy budget
365 decomposition are directly related to warming, and both decreasing the land surface albedo and
366 increasing land surface evaporative resistance lead to large-scale warming of the Earth system.

367 The mechanisms responsible for the surface warming are different; in the case of albedo, warming
368 is the direct result of increased *SW* absorption at the surface, while in the case of evaporative re-
369 sistance warming is the result of suppressed evaporative cooling and increased *SW* absorption due
370 to regional loss of cloud cover. However, in both cases, warming at the surface is accompanied by
371 warming aloft and an increase in atmospheric water vapour over large parts of the northern hemi-
372 sphere remote from the forcings (figure S8), presumably due to homogenization of atmospheric
373 temperature and moisture by basic state winds.

374 *e. Attribution of Zonal Mean ITCZ Shift*

375 In response to both decreased land surface albedo and increased land surface evaporative resis-
376 tance, there is a northwards shift in the ITCZ (figure ??a,b). Previous studies identified a strong
377 linear relationship between hemispheric energy imbalances, cross-equatorial atmospheric energy
378 transport, and the location of the ITCZ, both in models and in observations (?), with the ITCZ
379 shifting towards the hemisphere with the positive anomaly of net energy input (?????).

380 When land albedo is decreased, the Northern Hemisphere becomes the site of an anomalously
381 positive energy source as a result of increased absorption of *SW* by the larger land area in the
382 Northern Hemisphere. When land evaporative resistance is increased, loss of low cloud cover
383 in the northern mid-latitudes allows more sunlight to reach the surface over portions of northern
384 mid-latitude land, also resulting in an anomalously positive energy source in the Northern Hemi-
385 sphere. In both cases, the vertically integrated atmospheric energy budget balanced by a time-
386 mean decrease in atmospheric energy transport from the Southern Hemisphere into the Northern
387 Hemisphere, and a corresponding northwards shift in the zonal mean location of the ITCZ (figure
388 ??).

389 The relationship between annual mean cross-equatorial atmospheric energy transport and the
390 zonal mean ITCZ latitude ϕ_p is strongly linear in our simulations (figure ??). We find a -4.4° shift
391 in the ITCZ per 1 PW increase in annual mean northwards cross-equatorial atmospheric energy
392 transport (figure ??). This slope is slightly larger in magnitude than that found by ? across CMIP5
393 models ($-2.4^\circ/\text{PW}$) and from observations of the seasonal cycle in present-day climate ($-2.7^\circ/\text{PW}$).

394 The relationship between the zonal mean ITCZ location, ϕ_p , and cross-equatorial atmospheric
395 energy transport, AET_{eq} , in response to perturbed land surface properties is also tightly corre-
396 lated during Northern Hemisphere summer (figure ??a, c). However, we wish to decompose the
397 ITCZ shift into components associated with individual feedbacks (e.g. water vapor and Planck
398 feedbacks), which requires meridionally integrating the anomalous TOA energy flux due to each
399 feedback to obtain its contribution to the net cross-equatorial energy transport (e.g. ??); this can
400 only be done exactly in the annual mean, when the transient atmospheric storage term is zero in a
401 steady state climate. In order to leverage our decomposition of the TOA energy budget, we thus
402 focus our analysis of shifts in the ITCZ on the annual mean.

403 For each component of the TOA energy budget response to changes in land surface albedo and
404 evaporative resistance, we calculate the anomalous cross-equatorial energy flux needed to bal-
405 ance the specific pattern and magnitude of TOA SW and LW change comprising that component.
406 Then, using the linear relationship between cross-equatorial energy transport and ϕ_p , we quantify
407 how much of a shift in the ITCZ we would expect from each individual component of the TOA
408 energy budget response (figure S9 provides a heuristic illustration). Reducing albedo and increas-
409 ing evaporative resistance both drive northward shifts in cross-equatorial energy transport and the
410 ITCZ (figure ??, dark grey bars), but the processes responsible for these changes differ for the two
411 surface forcings. Since our primary interest is in the relative magnitudes of different feedbacks on

412 a given forcing, we rescale the net ITCZ shift produced by each imposed change in land surface
413 property so that it has a value of $+1^\circ$ (figure ??, dark gray bars).

414 Decreasing land albedo drives a northwards shift in the ITCZ as a result of the direct effect of the
415 imposed change in albedo, with positive (northward) contributions from the albedo feedback due
416 to changes in snow and ice, the *SW* and *LW* water vapour feedbacks, and the *LW* cloud feedback
417 (figure ??). It is notable that the *LW* cloud effects provide a negative feedback on the global
418 mean TOA energy balance response to the albedo forcing (Table 1) but a positive feedback on the
419 ITCZ response; this is the result of the specific pattern of the *LW* cloud feedback. Changes in
420 surface temperature, air temperature, and the *SW* effects of cloud cover changes all act as negative
421 feedbacks that reduce the northward shift of the ITCZ. Of all the feedbacks on the albedo forcing,
422 the Planck feedback is largest, consistent with global mean feedbacks on the CO_2 forcing of global
423 mean temperature; water vapor feedbacks are about an order of magnitude larger than the net cloud
424 feedback. The cloud feedbacks seem to be dominated by tropical cloud changes (figure ??f,g,h)
425 and exhibit strong cancellation between *SW* and *LW* components. The effect of all of the feedbacks
426 on the imposed change in land surface albedo largely cancel, such that the actual modelled shift
427 in the ITCZ is comparable to the shift in the ITCZ that would be realized by the *SW* effects of
428 the imposed change in land surface albedo alone. A similar cancellation of all feedbacks was seen
429 in the one-dimensional energy balance model of ?, although that model used an entirely oceanic
430 lower boundary and did not examine land surface forcings.

431 Increasing the evaporative resistance of land reduces terrestrial evaporation and leads to warm-
432 ing. There is no directly imposed change in TOA radiation that can be viewed as an imposed
433 forcing, but we are nevertheless able to quantify the contribution of each feedback to the total
434 ITCZ shift. The dominant positive contributors to the northwards shift of the ITCZ in response
435 to increased evaporative resistance are the change in TOA *SW* due to changes in cloud cover and

436 the change in TOA *LW* due to changes in water vapor. The water vapor-induced *LW* changes are
437 interesting because they result primarily from increases in humidity over the low-latitude oceans,
438 contrasting with the reduction in land humidity expected to result from an increase in land evapo-
439 rative resistance. The component that comes closest to constituting a forcing, from the perspective
440 of the energy budget, is the loss of low cloud cover in the northern midlatitudes, which results in a
441 hemispheric energy imbalance with more energy being added to the NH than the SH in response
442 to decreased land evaporation. Unlike in the case of albedo, the *LW* effects of changes in cloud
443 cover act in the same direction as the *SW* effects, although the *LW* cloud contribution is relatively
444 small. While changes in tropical clouds dominate the cloud feedbacks in response to a change
445 in land albedo, extra-tropical clouds dominate the cloud feedback in response to changes in land
446 evaporative resistance, with *SW* cloud effects greatly exceeding any cancellation from *LW* cloud
447 effects. Changes in TOA *SW* due to changes in cloud cover alone would result in a roughly 1.6°
448 northwards shift in the ITCZ, and the *LW* effect of changes in water vapor would drive an addi-
449 tion of 1.7° northwards shift, but this northwards shift is damped by a strong 3.0° southward shift
450 resulting from *LW* feedbacks driven by combined surface and atmospheric warming. While there
451 is a contribution to a northward ITCZ shift from loss of high-latitude snow and ice resulting from
452 warming, this contribution is smaller than the contributions from temperatures, water vapour, and
453 *SW* cloud feedbacks, and is not statistically significant.

454 The ITCZ shift predicted by the sum of the feedbacks is larger than the modelled ITCZ shift,
455 more so for evaporative resistance than for albedo (light gray bars in figure ??). This disagreement
456 is the result of the linear fit used to predict the ITCZ shift associated with a given change in cross-
457 equatorial energy transport not perfectly intersecting the interannual mean of the three model
458 simulations (compare dashed line to large markers in figure ??a). However, we note that since
459 these are re-scaled values and the net zonal-mean, model-simulated ITCZ shift for the evaporative

460 resistance forcing is only about 0.3° in a model with a horizontal grid spacing of about 2° , this
461 non-linearity may be negligible compared to discretization and other numerical uncertainties.

462 **4. Summary and Discussion**

463 Both albedo and evaporative resistance of the land surface can drive large changes in the TOA
464 radiation balance. However, the pathways through which these land surface properties modify
465 the TOA radiative budget differ. This study provides a breakdown of the impact of individual
466 land surface property changes on TOA radiation, zonally averaged AET_{eq} , and zonal mean ITCZ
467 location. We leverage atmospheric radiative kernels to decompose the effect of decreasing land
468 surface albedo and increasing land surface evaporative resistance on the TOA energy balance.

469 Decreasing land surface albedo leads to an overall increase in energy absorbed at the TOA over
470 land regions, and a compensating increase in energy lost from the TOA over ocean regions. The
471 surface warming caused by the imposed reduction in surface albedo leads to reduced snow and
472 ice cover that, in turn, cause even more SW to be absorbed by the Earth system. The LW effects
473 of changes in atmospheric water vapor driven by the reduction in land surface albedo also lead to
474 an increase in energy absorbed at the TOA, while warming of surface and air temperatures and
475 changes in cloud cover lead to energy loss from the TOA.

476 Changes in land surface albedo are strongly attenuated by the atmosphere. That is, for a given
477 change in surface albedo, the change in planetary albedo (the fraction of insolation not absorbed
478 by the climate system) is much smaller (?). Nonetheless, we have demonstrated that changes in
479 land surface albedo can modify TOA net radiation not only directly by modifying the net flux of
480 SW radiation, but also indirectly by modifying atmospheric temperatures, water vapor content,
481 cloud cover, etc. Furthermore, land albedo changes can produce shifts in atmospheric circulations
482 and rainfall, even if their influence on global mean planetary albedo is modest.

483 Increasing land surface evaporative resistance primarily impacts the TOA radiative budget over
484 northern mid-latitude land regions. The *SW* effect of changes in cloud cover is the most direct
485 effect of the imposed increase in evaporative resistance, presumably resulting from reductions in
486 cloud cover caused by reduced humidity in the region of the forcing. Planck and water vapor
487 feedbacks act on this forcing in a similar way as for the albedo forcing; these feedbacks are geo-
488 graphically remote and have patterns of TOA energy flux change that are highly correlated for the
489 two forcings.

490 We use the relationship between cross-equatorial energy transport, as diagnosed from TOA en-
491 ergy fluxes, and the zonal mean location of the ITCZ to attribute northward shifts in precipitation
492 to individual surface and atmospheric responses to imposed land surface changes. The combined
493 effect of all atmospheric feedbacks on an imposed change in land surface albedo largely cancel,
494 and the resulting northward shift in the ITCZ is the same shift you would expect from the *SW*
495 effects of the imposed change in albedo alone. For the imposed increase in evaporative resistance,
496 the *SW* effect of clouds, combined with albedo changes due to reduced snow and ice cover as
497 a result of warming, results in a net northward shift in the ITCZ. For the evaporative resistance
498 forcing, the *SW* effect of clouds on ITCZ location is in the opposite direction as the *SW* effect of
499 clouds for the albedo forcing.

500 The idealized nature of these simulations necessarily presents some limitations. The perturba-
501 tions made to land surface albedo and evaporative resistance were applied to all non-glaciated land
502 surfaces, and as such the hemispheric imbalance in response to these land surface perturbations is
503 largely a result of the hemispherically asymmetric distribution of the continents in their present-
504 day configuration; other patterns of land surface change would yield their own specific patterns
505 of TOA energy flux changes and individual forcing/feedback terms. The radiative kernel we use
506 to decompose the TOA energy budget response into its components was generated with the same

507 atmospheric model as we use in this study (CAM5). However, any differences in the mean state of
508 atmospheric temperatures, humidity, and cloud cover between the CLM-CAM5 simulation used
509 for the kernels and the baseline SLIM-CAM5 simulation used in this study could introduce errors
510 in the kernel-predicted change in TOA radiation. Furthermore, because we do not have an explicit
511 radiative kernel for cloud fraction, any residuals that may exist in our calculations are lumped in
512 with the impact of clouds on TOA *SW* and *LW*, by virtue of the methods we use to decompose
513 the TOA energy balance (see Appendix). However, we expect these residuals to be small for two
514 reasons: (a) the mean state of SLIM-CAM5 is similar to the mean state of CLM-CAM5 (? see)
515 and (b) the patterns of ΔSW_{cloud} and ΔLW_{cloud} strongly resemble the change in cloud fraction in
516 our simulations, supporting the idea that they indeed result from changes in cloud cover. Another
517 important caveat is that we use a single atmospheric model and a single radiative kernel in this
518 study. While the direct effect of surface albedo on TOA *SW* radiation under clear-sky conditions
519 is similar across radiative kernels from multiple models (????), the response of cloud cover to a
520 perturbation can vary widely across models (?). Particularly for the evaporative resistance forc-
521 ing, for which cloud changes are the dominant driver of changes in the TOA radiative budget, other
522 atmospheric models could generate different patterns of TOA *SW* and *LW* response. Finally, we
523 focused on changes in zonal mean tropical rainfall, and it is known that zonal mean changes are
524 not generally representative of regional precipitation change (??); we leave a detailed exploration
525 of the zonally resolved response for separate work.

526 Despite these caveats, the method we present here allows us to understand the mechanisms
527 through which changes in the land surface drive changes in zonal mean atmospheric circulation and
528 tropical precipitation. Understanding these mechanisms is critical to understanding how changes
529 in the land surface—both historical and in the future—impact climate locally and globally.

530 **5. Data Availability**

531 The data presented in this paper will be archived on Dryad and the link added here upon accep-
532 tance of this manuscript. The source code for the models used in this study are publicly available
533 on github at https://escomp.github.io/CESM/release-cesm2/downloading_cesm.html
534 for CESM, and <https://github.com/marysa/SimpleLand> for SLIM.

535 *Acknowledgments.* MML acknowledges postdoctoral funding support from the James S. Mc-
536 Donnell Foundation Postdoctoral Fellowship in Dynamic and Multiscale Systems and NSERC
537 Grant PGSD3-487470- 2016. MML and ALSS acknowledge support from NSF Grant 1553715
538 to the University of Washington. WRB acknowledges support from the U.S. Department
539 of Energy, Office of Science, Office of Biological and Environmental Research, Climate
540 and Environmental Sciences Division, Regional and Global Model Analysis Program, under
541 Award DE-SC0019367. We acknowledge high-performance computing support from Cheyenne
542 (doi:10.5065/D6RX99HX) provided by NCAR's Computational and Information Systems Lab-
543 oratory, sponsored by the National Science Foundation. We acknowledge additional comput-
544 ing resources from the National Energy Research Scientific Computing Center (NERSC), a U.S.
545 Department of Energy Office of Science User Facility operated under Contract No. DE-AC02-
546 05CH11231.

548 *a. TOA Energy Budget*

549 Decreasing land surface albedo or increasing land surface evaporative resistance modifies the
550 energy balance at the surface (SFC_{net}) and top of atmosphere (TOA_{net}) (equations ??-??).

$$TOA_{net} = SW_{TOA}^{\downarrow} - SW_{TOA}^{\uparrow} - LW_{TOA}^{\uparrow} \quad (A1)$$

$$SFC_{net} = SW_{SFC}^{\downarrow} - SW_{SFC}^{\uparrow} + LW_{SFC}^{\downarrow} - LW_{SFC}^{\uparrow} \\ - SH_{SFC} - LH_{SFC} \quad (A2)$$

551 At the TOA, the energy balance is between incoming shortwave (SW) radiation, reflected SW
552 radiation, and outgoing longwave radiation (LW). At the surface, the balance is between the net
553 flux of SW and LW radiation, and the turbulent fluxes of sensible heat (SH) and latent heat (LH).
554 The sign convention in equations ??-?? is such that $SFC_{net} > 0$ means more energy absorbed
555 by the surface (land or ocean). More energy is absorbed by the Earth system in regions with
556 $TOA_{net} > 0$, while more energy is lost by the Earth system in regions with $TOA_{net} < 0$. On land
557 over sufficiently long timescales (e.g. the annual mean, which we examine here), the surface
558 energy budget balances, such that $SFC_{net} = 0$. The slab ocean model used in these simulations has
559 the same prescribed heat transport across all simulations; $SFC_{net} > 0$ in regions where the ocean
560 takes up atmospheric energy, and $SFC_{net} < 0$ in regions where the ocean releases energy to the
561 atmosphere.

562 Independent of any atmospheric feedbacks, a decrease in land albedo results in more shortwave
563 energy absorbed at the land surface, with a corresponding increase in the upwards surface energy
564 fluxes. In contrast, an increase in land evaporative resistance does not directly change the total
565 amount of energy absorbed or emitted by the land surface; rather, increasing evaporative resistance
566 reduces evaporation (i.e. reduces the latent heat flux), while sensible heat and upwards longwave
567 radiation increase to balance the surface energy budget. However, atmospheric responses to land

568 surface changes can modify both the downward fluxes of SW and LW at the surface, and the
 569 outgoing fluxes of SW and LW at the TOA.

570 *b. Atmospheric Energy Transport*

571 We can calculate changes in atmospheric energy transport at the equator using two separate
 572 approaches. In the annual mean only, we use changes in TOA_{net} and SFC_{net} (equation ??) (?).

$$\begin{aligned}
 AET_{eq} &= \int_0^{2\pi} \int_{-\frac{\pi}{2}}^0 2\pi a^2 \cos \phi (TOA_{net} - SFC_{net}) d\phi d\lambda \\
 &= - \int_0^{2\pi} \int_0^{\frac{\pi}{2}} 2\pi a^2 \cos \phi (TOA_{net} - SFC_{net}) d\phi d\lambda
 \end{aligned}
 \tag{A3}$$

573 $AET_{eq} > 0$ means positive energy transport by the atmosphere from the Southern to Northern
 574 Hemisphere. Cross-equatorial atmospheric heat transport can also be calculated directly from the
 575 meridional transport of moist static energy within the atmosphere evaluated at the equator $\langle vh \rangle_0$
 576 (equation ??).

$$\langle vh \rangle_0 = \left(\frac{1}{g} \int_{sfc}^{TOA} vh \right) \Big|_{lat=0}
 \tag{A4}$$

$$h = c_p T + L_v Q + gZ
 \tag{A5}$$

577 where v is the meridional wind and h is the moist static energy. vh is calculated from the heat
 578 capacity of dry air c_p , the latent heat of vapourization L_v , the meridional atmospheric transport
 579 of heat vT , the meridional atmospheric transport of moisture vQ , and the meridional transport of
 580 potential energy vZ . In the annual mean, AET_{eq} calculated from the TOA energy budget is identical
 581 to $\langle vh \rangle_0$ calculated from vertically integrated atmospheric energy and winds. However, at sub-
 582 annual timescales, heat storage within the surface and the atmosphere cause AET (implied from
 583 the TOA energy budget) to differ substantially from $\langle vh \rangle$ (actual/explicitly calculated atmospheric
 584 energy transport). Thus, the relationship between AET_{eq} and ϕ_p is only valid at annual mean
 585 timescales, while the relationship between $\langle vh \rangle_0$ and ϕ_p is valid on seasonal timescales as well

586 (figure ??). However, we focus on annual mean AET_{eq} in this study in order to make use of
587 changes in TOA radiation driven by specific atmospheric and surface processes.

588 Each of the individual forcing and feedback terms explored in this study modify the TOA energy
589 imbalance. Using the contribution of each term to TOA_{net} , we leverage equation ?? to quantify
590 the contribution of each forcing and feedback to AET_{eq} .

591 *c. Relationship between AET_{eq} and ϕ_p*

592 In the annual mean, the relationship between AET_{eq} and ϕ_p is the same as that between $\langle vh \rangle_0$
593 and ϕ_p : both methods give a strongly linear relationship, with roughly 4.2 PW of southwards
594 atmospheric energy transport (as calculated by $\langle vh \rangle_0$) corresponding to a 1° northwards shift in
595 the ITCZ, and with roughly 4.4 PW of southwards atmospheric energy transport (as calculated
596 from the TOA energy budget) corresponding to a 1° northwards shift in the ITCZ. However, due
597 to heat storage by the surface and atmosphere, AET (inferred from TOA_{net}) deviates substantially
598 from actual atmospheric energy transport $\langle vh \rangle$ at sub-annual timescales. Thus, we cannot consider
599 the relationship between AET_{eq} and ϕ_p at sub-annual timescales. Indeed, as noted in figure ??,
600 relationship between cross-equatorial atmospheric heat transport and ϕ_p differ between the AET
601 and $\langle vh \rangle$ approaches at sub-annual timescales, particularly for DJF. While we *can* consider the
602 relationship between $\langle vh \rangle_0$ and ϕ_p at sub-annual timescales, here we require the use of the AET_{eq}
603 approach, as we decompose the effect of individual surface and atmospheric processes on TOA_{net} .
604 Thus, we present our analysis for annual mean timescales only.

605 *d. Radiative kernel calculations*

606 We use a radiative kernel to diagnose the change in TOA_{net} resulting from the imposed change
607 in surface albedo, the change in surface albedo resulting from changes in snow and ice, the change

608 in surface temperature, the change in the vertical profile of air temperatures, and the change in the
609 vertical profile of atmospheric water vapour (??). Specifically, we leverage the radiative kernel
610 from ?, which uses the same atmospheric model (CAM5) as this study.

611 The kernel K gives the change in surface and TOA net SW and/or LW radiation resulting from a
612 1% change in surface albedo, a 1K change in surface temperature T_s , a 1K change in air tempera-
613 ture T at every vertical model level, and a change in water vapour q at every vertical model level
614 equivalent to a 1K increase in air temperature while maintaining constant relative humidity. The
615 kernel provides calculations for both “full sky” and “clear sky” conditions. The full sky kernel
616 gives the change in radiative fluxes resulting from each perturbation assuming cloud cover does
617 not change (but still allowing for the effects of climatological cloud cover). The clear sky kernel
618 gives the change in radiative fluxes resulting from each perturbation assuming there are no clouds
619 present. For our calculations, we focus on (a) the full sky radiative kernel and (b) the response of
620 TOA (not surface) SW and LW fluxes.

621 We use the following notation when referring to calculations using the radiative kernel. The
622 change in net TOA SW as a result of a 1% change in surface albedo is given by K_α . The change
623 in net TOA LW resulting from a 1K increase in surface temperature is given by K_{T_s} . The change
624 in TOA LW resulting from a 1K increase in air temperature vertically through the atmosphere is
625 given by K_T . The change in TOA SW and LW resulting from the imposed change in water vapour
626 are given by $K_{q,SW}$ and $K_{q,LW}$, respectively.

627 We impose a change in snow-free albedo $\Delta\alpha_i$ on the land surface. Using $\Delta\alpha_i$, we can quantify
628 the change in top of atmosphere SW radiation directly attributable to the imposed change in surface
629 albedo ΔSW_{α_i} (equation ??), where $\Delta\alpha_i$ is multiplied by 100 to convert it to a percent value.

$$\Delta SW_{\alpha_i} = K_\alpha \times 100 \times \Delta\alpha_i \quad (\text{A6})$$

630 The total modeled change in albedo includes both our imposed snow-free change in albedo as
 631 well as albedo changes due to snow and ice responses. We can calculate the change in albedo due to
 632 snow and ice changes (α_s) by subtracting the imposed change in albedo α_i from the actual modeled
 633 change in albedo α_m (figure S2; see also supplemental section ??). The change in albedo resulting
 634 from changes in snow and ice α_s is then multiplied by the radiative kernel to get the change in net
 635 TOA *SW* radiation resulting from albedo changes from snow and ice, ΔSW_{α_s} (equation ??).

$$\Delta SW_{\alpha_s} = K_{\alpha} \times 100 \times \Delta \alpha_s \quad (\text{A7})$$

636 Changes in surface temperature impact net TOA *LW* radiation; we determine how the specific
 637 surface temperature response to each land surface property change impacts TOA *LW* (ΔLW_{T_s}) using
 638 the radiative kernel for surface temperature (equation ??).

$$\Delta LW_{T_s} = K_{T_s} \times \Delta T_s \quad (\text{A8})$$

639 Changes in air temperature throughout the atmospheric column modify both the upwards and
 640 downwards flux of *LW* radiation through the atmosphere. Here, we are specifically interested
 641 in how changes in air temperature throughout the atmospheric column modify *LW* at the TOA
 642 (ΔLW_T). We multiply the radiative kernel for temperature by the change in temperature, then sum
 643 over the atmospheric column to get the total effect of the air temperature changes at all vertical
 644 levels on TOA *LW* (equation ??).

$$\Delta LW_{\Delta T} = \sum_{SFC}^{TOA} K_T \times \Delta T \quad (\text{A9})$$

645 Changes in atmospheric water vapour q modulate both *SW* and *LW* radiation. As with changes
 646 in T , we are interested in the vertical sum of the effect of Δq on TOA *SW* and *LW*. The raw
 647 kernel for water vapour K_q gives the change in radiative fluxes for the change in q associated
 648 with a 1K temperature change at constant relative humidity, while our simulations provide us

649 with a Δq . Thus, we follow the methodology presented by ? to calculate an intermediate kernel
650 $K_q^* = K_q / \frac{\delta q}{\Delta T}$, where δT is the modelled change in air temperature and δq is the change in specific
651 humidity that would have resulted from ΔT given constant relative humidity. Then, we can use
652 K_q^* to determine the change in TOA SW and LW attributable to the modelled change in specific
653 humidity Δq (equations ??-??).

$$\Delta SW_{\Delta q} = \sum_{SFC}^{TOA} K_{q,SW}^* \times \Delta q \quad (A10)$$

$$\Delta LW_{\Delta q} = \sum_{SFC}^{TOA} K_{q,LW}^* \times \Delta q \quad (A11)$$

654 e. Clouds

655 To determine the effect of changes in cloud cover on TOA_{net} , we do not use a radiative kernel
656 for cloud cover. Rather, we determine how much the modelled change in cloud fraction impacts
657 SW and LW at the TOA, by calculating the total modelled response of TOA_{net} then subtract the
658 change in TOA_{net} due to the combined effects of albedo, temperature, and water vapour (equations
659 ??-??).

$$\begin{aligned} \Delta SW_{cloud} = & \Delta SW_{model} - K_{\alpha} \times \Delta \alpha_i \\ & - K_{\alpha} \times \Delta \alpha_s - \sum_{sfc}^{toa} K_{q,SW} \times \Delta q \end{aligned} \quad (A12)$$

$$\begin{aligned} \Delta LW_{cloud} = & \Delta LW_{model} - K_{T_s} \times \Delta T_s \\ & - \sum_{sfc}^{toa} K_T \times \Delta T - \sum_{sfc}^{toa} K_{q,LW} \times \Delta q \end{aligned} \quad (A13)$$

661 Because we do not diagnose ΔLW_{cloud} or ΔSW_{cloud} directly from a cloud kernel, the ΔLW_{cloud} or
662 ΔSW_{cloud} terms necessarily also include any potential residual terms associated with the kernel.
663 That is, if the actual direct response of TOA SW to $\Delta \alpha_i$ in our simulations differs from the ΔSW_{α_i}
664 predicted by K_{α} because, for example, the mean state of cloud cover in our SLIM-CAM5 sim-

665 ulations differs substantially from the mean state of cloud cover in the CLM-CAM5 model, that
666 difference would necessarily be included in the ΔSW_{cloud} and ΔLW_{cloud} terms here.

667 We also consider changes in the shortwave cloud forcing ($SWCF$) and longwave cloud forcing
668 ($LWCF$). This is a different quantity than ΔSW_{cloud} and ΔLW_{cloud} (see, for example, figure 11 in
669 ?). ΔSW_{cloud} and ΔLW_{cloud} are the change in TOA SW and LW radiation due to the change in cloud
670 cover resulting from our imposed land surface property change. In contrast, the $SWCF$ and $LWCF$
671 quantify the difference in TOA SW and LW radiation between cloudy (full sky) and cloud-free
672 (clear sky) conditions (equation ??-??).

$$SWCF = SW_{clearsky} - SW_{fullsky} \quad (A14)$$

$$LWCF = LW_{fullsky} - LW_{clearsky} \quad (A15)$$

673 Note the different order of the full sky and clear sky terms for $SWCF$ vs. $LWCF$. This is because
674 TOA SW (LW) fluxes are, by convention, positive downwards (upwards). This definition of $SWCF$
675 and $LWCF$ is such that positive values indicate more energy into the system as a result of cloud
676 cover. Over land, $SWCF$ is usually negative because clouds reflect sunlight, while $LWCF$ is usu-
677 ally positive because cloud tops tend to radiate at cooler temperatures than the ground below them.
678 The *change* in $SWCF$ and $LWCF$ as a result of changes in land surface properties can occur with-
679 out any change in cloud cover (e.g. changing land surface albedo modifies $SW_{clearsky}$ and thus
680 $SWCF$), but can also occur as a result of changes in cloud cover.

681 **References**

682 Andrews, T., J. M. Gregory, M. J. Webb, and K. E. Taylor, 2012: Forcing, feedbacks and climate
683 sensitivity in CMIP5 coupled atmosphere-ocean climate models. *Geophysical Research Letters*,
684 **39** (9), 1–7, doi:10.1029/2012GL051607.

- 685 Atwood, A. R., A. Donohoe, D. S. Battisti, X. Liu, and F. S. R. Pausata, 2020: Robust
686 longitudinally-variable responses of the ITCZ to a myriad of climate forcings. *Geophysical*
687 *Research Letters*, **47** (17), 1–13, doi:10.1029/2020GL088833.
- 688 Bailey, D., E. Hunke, A. DuVivier, B. Lipscomb, C. Bitz, M. Holland, B. Briegleb, and
689 J. Schramm, 2018: CESM CICE5 Users Guide. Tech. rep., 47 pp. URL [https://buildmedia.](https://buildmedia.readthedocs.org/media/pdf/cesmcice/latest/cesmcice.pdf)
690 [readthedocs.org/media/pdf/cesmcice/latest/cesmcice.pdf](https://buildmedia.readthedocs.org/media/pdf/cesmcice/latest/cesmcice.pdf).
- 691 Betts, A. K., J. H. Ball, A. C. Beljaars, M. J. Miller, and P. A. Viterbo, 1996: The land surface-
692 atmosphere interaction: A review based on observational and global modeling perspectives.
693 *Journal of Geophysical Research Atmospheres*, **101** (D3), 7209–7225, doi:10.1029/95JD02135.
- 694 Bonan, G., 2016: *Ecological Climatology*. 3rd ed., Cambridge University Press, doi:10.1017/
695 [cbo9781107339200](https://doi.org/10.1017/cbo9781107339200).
- 696 Bonan, G. B., 2008: *Ecological Climatology*. Cambridge Univ. Press, Cambridge, UK.
- 697 Bonan, G. B., D. Pollard, and S. L. Thompson, 1992: Effects of boreal forest vegetation on global
698 climate. *Nature*, **359** (6397), 716–718, doi:Doi10.1038/359716a0.
- 699 Broccoli, A. J., K. a. Dahl, and R. J. Stouffer, 2006: Response of the ITCZ to Northern Hemisphere
700 cooling. *Geophysical Research Letters*, **33** (1), 1–4, doi:10.1029/2005GL024546.
- 701 Broccoli, A. J., and S. Manabe, 1987: The influence of continental ice, atmospheric CO₂, and
702 land albedo on the climate of the last glacial maximum. *Climate Dynamics*, **1** (2), 87–99, doi:
703 [10.1007/BF01054478](https://doi.org/10.1007/BF01054478).
- 704 Budyko, M. I., 1961: The Heat Balance of the Earth's Surface. *Soviet Geography*, **2** (4), 3–13,
705 doi:10.1080/00385417.1961.10770761.

706 Budyko, M. I., 1969: The effect of solar radiation variations on the climate of the Earth. *Tellus*,
707 **21 (5)**, 611–619, doi:10.3402/tellusa.v21i5.10109.

708 Budyko, M. I., 1982: The Earth's climate: past and future. *The Earth's climate: past and future.*,
709 doi:10.1016/0004-6981(83)90167-1.

710 Byrne, M. P., and P. A. O’Gorman, 2015: The response of precipitation minus evapotranspiration
711 to climate warming: Why the "Wet-get-wetter, dry-get-drier" scaling does not hold over land.
712 *Journal of Climate*, **28 (20)**, 8078–8092, doi:10.1175/JCLI-D-15-0369.1.

713 Cess, R. D., and S. D. Goldenberg, 1981: The effect of ocean heat capacity upon global warming
714 due to increasing atmospheric carbon dioxide. *Journal of Geophysical Research*, **86 (80)**, 498–
715 502.

716 Charney, J., W. J. Quirk, S.-H. Chow, and J. Kornfield, 1977: A comparative study of the effects
717 of albedo change on drought in semi-arid regions. doi:10.1175/1520-0469(1977)034<1366:
718 ACSOTE>2.0.CO;2.

719 Charney, J., P. H. Stone, and W. J. Quirk, 1975: Drought in Sahara - Biogeophysical Feedback
720 Mechanism. *Science*, **187 (4175)**, 434–435, doi:doi:10.1126/science.187.4175.434.

721 Chiang, J. C. H., and C. M. Bitz, 2005: Influence of high latitude ice cover on the marine Intertrop-
722 ical Convergence Zone. *Climate Dynamics*, **25 (5)**, 477–496, doi:10.1007/s00382-005-0040-5.

723 Cvijanovic, I., and J. C. Chiang, 2013: Global energy budget changes to high latitude North
724 Atlantic cooling and the tropical ITCZ response. *Climate Dynamics*, **40 (5-6)**, 1435–1452, doi:
725 10.1007/s00382-012-1482-1.

726 Davin, E. L., N. de Noblet-Ducoudré, N. de Noblet-Ducoudre, and N. de Noblet-Ducoudré, 2010:
727 Climatic Impact of Global-Scale Deforestation: Radiative versus Nonradiative Processes. *Jour-*

728 *nal of Climate*, **23** (1), 97–112, doi:10.1175/2009JCLI3102.1, URL [http://journals.ametsoc.org/](http://journals.ametsoc.org/doi/abs/10.1175/2009JCLI3102.1)
729 [doi/abs/10.1175/2009JCLI3102.1](http://journals.ametsoc.org/doi/abs/10.1175/2009JCLI3102.1).

730 Devaraju, N., N. de Noblet-Ducoudré, B. Quesada, and G. Bala, 2018: Quantifying the relative
731 importance of direct and indirect biophysical effects of deforestation on surface temperature and
732 teleconnections. *Journal of Climate*, **31** (10), 3811–3829, doi:10.1175/JCLI-D-17-0563.1.

733 Dickinson, R. E., 1983: Land surface processes and climate—surface albedos and energy balance.
734 *Advances in Geophysics*, **25** (C), 305–353, doi:10.1016/S0065-2687(08)60176-4.

735 Donohoe, A., and D. S. Battisti, 2011: Atmospheric and surface contributions to planetary albedo.
736 *Journal of Climate*, **24** (16), 4402–4418, doi:10.1175/2011JCLI3946.1.

737 Donohoe, A., J. Marshall, D. Ferreira, and D. Mcgee, 2013: The relationship between ITCZ
738 location and cross-equatorial atmospheric heat transport: From the seasonal cycle to the last
739 glacial maximum. *Journal of Climate*, **26** (11), 3597–3618, doi:10.1175/JCLI-D-12-00467.1.

740 Flanner, M. G., K. M. Shell, M. Barlage, D. K. Perovich, and M. A. Tschudi, 2011: Radiative
741 forcing and albedo feedback from the Northern Hemisphere cryosphere between 1979 and 2008.
742 *Nature Geoscience*, **4** (3), 151–155, doi:10.1038/ngeo1062.

743 Geen, R., S. Bordoni, D. Battisti, and K. Hui, 2020: The Dynamics of the Global Monsoon -
744 Connecting Theory and Observations. *Earth and Space Science Open Archive*, 1–26, doi:<https://doi.org/10.1002/essoar.10502409.1>.

745

746 Hurrell, J. W., and Coauthors, 2013: The Community Earth System Model: A Framework for
747 Collaborative Research. *Bulletin of the American Meteorological Society*, **94** (9), 1339–1360,
748 doi:10.1175/BAMS-D-12-00121.1, URL <https://doi.org/10.1175/BAMS-D-12-00121.1>.

749 Kang, S. M., 2020: Extratropical Influence on the Tropical Rainfall Distribution. **1**, 24–36.

- 750 Kang, S. M., D. M. W. Frierson, and I. M. Held, 2009: The Tropical Response to Extrat-
751 ropical Thermal Forcing in an Idealized GCM: The Importance of Radiative Feedbacks and
752 Convective Parameterization. *Journal of the Atmospheric Sciences*, **66** (9), 2812–2827, doi:
753 10.1175/2009JAS2924.1.
- 754 Kang, S. M., I. M. Held, D. M. W. Frierson, and M. Zhao, 2008: The Response of the ITCZ
755 to Extratropical Thermal Forcing: Idealized Slab-Ocean Experiments with a GCM. *Journal of*
756 *Climate*, **21** (14), 3521–3532, doi:10.1175/2007JCLI2146.1.
- 757 Kooperman, G. J., Y. Chen, F. M. Hoffman, C. D. Koven, K. Lindsay, M. S. Pritchard, A. L.
758 Swann, and J. T. Randerson, 2018: Forest response to rising CO₂ drives zonally asymmet-
759 ric rainfall change over tropical land. *Nature Climate Change*, **8** (5), 434–440, doi:10.1038/
760 s41558-018-0144-7, URL <http://dx.doi.org/10.1038/s41558-018-0144-7>.
- 761 Koster, R., and Coauthors, 2004: Regions of Strong Coupling Between Soil Moisture and Precip-
762 itation. *Science*, **305**, 1138–1140.
- 763 Koster, R. D., and Coauthors, 2006: GLACE: The Global Land-Atmosphere Coupling Experi-
764 ment. Part I: Overview. *Journal of Hydrometeorology*, **7** (4), 590–610, doi:10.1175/JHM510.1.
- 765 Laguë, M. M., G. B. Bonan, and A. L. S. Swann, 2019: Separating the Impact of Individual
766 Land Surface Properties on the Terrestrial Surface Energy Budget in both the Coupled and
767 Uncoupled Land–Atmosphere System. *Journal of Climate*, **32** (18), 5725–5744, doi:10.1175/
768 jcli-d-18-0812.1.
- 769 Laguë, M. M., and A. L. S. Swann, 2016: Progressive Mid-latitude Afforestation: Impacts on
770 Clouds, Global Energy Transport, and Precipitation. *Journal of Climate*, **29** (15), 5561–5573,
771 doi:10.1175/JCLI-D-15-0748.1, URL <http://dx.doi.org/10.1175/JCLI-D-15-0748.1>.

772 Lawrence, D. M., and Coauthors, 2019: The Community Land Model Version 5: Description
773 of New Features, Benchmarking, and Impact of Forcing Uncertainty. *Journal of Advances in*
774 *Modeling Earth Systems*, **11** (12), 4245–4287, doi:10.1029/2018MS001583.

775 Lee, X., and Coauthors, 2011: Observed increase in local cooling effect of deforestation at higher
776 latitudes. *Nature*, **479** (7373), 384–387, doi:10.1038/nature10588, URL <http://dx.doi.org/10.1038/nature10588>.

778 Lintner, B. R., A. B. Gilliland, and I. Y. Fung, 2004: Mechanisms of convection-induced modula-
779 tion of passive tracer interhemispheric transport interannual variability. *Journal of Geophysical*
780 *Research D: Atmospheres*, **109** (13), 1–13, doi:10.1029/2003JD004306.

781 Manabe, S., 1969: Climate and the Ocean Circulation 1. *Monthly Weather Review*, **97** (11), 739–
782 774, doi:10.1175/1520-0493(1969)097<0739:CATOC>2.3.CO;2, URL [http://journals.ametsoc.org/doi/abs/10.1175/1520-0493\(1969\)097%3C0739:CATOC%3E2.3.CO;2](http://journals.ametsoc.org/doi/abs/10.1175/1520-0493(1969)097%3C0739:CATOC%3E2.3.CO;2).

784 Milly, P. C. D., and a. B. Shmakin, 2002: Global Modeling of Land Water and Energy Balances.
785 Part I: The Land Dynamics (LaD) Model. *Journal of Hydrometeorology*, **3** (3), 283–299, doi:10.
786 1175/1525-7541(2002)003<0283:GMOLWA>2.0.CO;2, URL <http://journals.ametsoc.org/doi/abs/10.1175/1525-7541%282002%29003%3C0283%3AGMOLWA%3E2.0.CO%3B2>.

788 Neale, R. B., and Coauthors, 2012: Description of the NCAR community atmosphere model
789 (CAM 5.0). *NCAR Tech. Note NCAR/TN-486+STR*.

790 North, G. R., J. G. Mengel, and D. A. Short, 1983: Simple energy balance model resolving the
791 seasons and the continents: application to the astronomical theory of the ice ages. *Journal of*
792 *Geophysical Research*, **88** (C11), 6576–6586, doi:10.1029/JC088iC11p06576.

- 793 Oleson, K. W., and Coauthors, 2013: Technical Description of version 4.5 of the Community
794 Land Model (CLM). *NCAR Tech. Note NCAR/TN-503+STR*, (July), NCAR/TN-503+STR,
795 URL [http://www.cesm.
796 ucar.edu/models/cesm1.2/clm/](http://www.cesm.ucar.edu/models/cesm1.2/clm/CLM45_Tech_Note.pdf).
- 797 Payne, R. E., 1972: Albedo of the Sea Surface. 959–970 pp., doi:10.1175/1520-0469(1972)
798 029(0959:aotss)2.0.co;2.
- 799 Pendergrass, A. G., A. Conley, and F. M. Vitt, 2018: Surface and top-of-Atmosphere radiative
800 feedback kernels for cesm-cam5. *Earth System Science Data*, **10** (1), 317–324, doi:10.5194/
801 essd-10-317-2018.
- 802 Peterson, H. G., and W. R. Boos, 2020: Feedbacks and eddy diffusivity in an energy balance
803 model of tropical rainfall shifts. *npj Climate and Atmospheric Science*, **3** (1), 1–10, doi:10.
804 1038/s41612-020-0114-4, URL <http://dx.doi.org/10.1038/s41612-020-0114-4>.
- 805 Sellers, P. J., and Coauthors, 1996: Comparison of radiative and physiological effects of dou-
806 bled atmospheric CO₂ on climate. *SCIENCE-NEW YORK THEN WASHINGTON-*, **271** (5254),
807 1402–1405, doi:10.1126/science.271.5254.1402.
- 808 Shell, K. M., J. T. Kiehl, and C. A. Shields, 2008: Using the radiative kernel technique to calculate
809 climate feedbacks in NCAR’s Community Atmospheric Model. *Journal of Climate*, **21** (10),
810 2269–2282, doi:10.1175/2007JCLI2044.1.
- 811 Shukla, J., and Y. Mintz, 1982: Influence of Land-Surface Evapotranspiration on the Earth’s Cli-
812 mate. *Science*, **215** (4539), 1498–1501.

813 Soden, B. J., and I. M. Held, 2006: An Assessment of Climate Feedbacks in Coupled Ocean–
814 Atmosphere Models. *Journal of Climate*, **19** (14), 3354–3360, doi:10.1175/JCLI3799.1, URL
815 <http://dx.doi.org/10.1175/JCLI3799.1>.

816 Soden, B. J., I. M. Held, R. Colman, K. M. Shell, J. T. Kiehl, and C. A. Shields, 2008: Quantifying
817 Climate Feedbacks Using Radiative Kernels. *Journal of Climate*, **21** (14), 3504–3520, doi:10.
818 1175/2007JCLI2110.1, URL <http://journals.ametsoc.org/doi/abs/10.1175/2007JCLI2110.1>
819 <http://dx.doi.org/10.1175/2007JCLI2110.1>.

820 Stocker, T. F., and Coauthors, 2013: Climate change 2013 the physical science basis: Working
821 Group I contribution to the fifth assessment report of the Intergovernmental Panel on Climate
822 Change. *Contribution of Working Group I to the Fifth Assessment Report of the Intergovern-
823 mental Panel on Climate Change.*, **9781107057**, 1–1535, doi:10.1017/CBO9781107415324.

824 Swann, A. L. S., I. Y. Fung, and J. C. H. Chiang, 2012: Mid-latitude afforestation shifts general
825 circulation and tropical precipitation. *Proceedings of the National Academy of Sciences*, **109** (3),
826 712–716, doi:10.1073/pnas.1116706108.

827 Winckler, J., and Coauthors, 2018: Different response of surface temperature and air temperature
828 to deforestation in climate models. *Earth System Dynamics Discussions*, 1–17, doi:10.5194/
829 esd-2018-66.

830 Zarakas, C. M., A. L. Swann, M. M. Laguë, K. C. Armour, and J. T. Randerson, 2020: Plant
831 Physiology Increases the Magnitude and Spread of the Transient Climate Response to CO₂ in
832 CMIP6 Earth System Models. *Journal of Climate*, 1–44, doi:10.1175/jcli-d-20-0078.1.

833 Zelinka, M. D., D. A. Randall, M. J. Webb, and S. A. Klein, 2017: Clearing clouds of uncertainty.
834 *Nature Climate Change*, **7** (10), 674–678, doi:10.1038/nclimate3402.

835 **LIST OF TABLES**

836 **Table 1.** Table of the globally averaged annual mean (and standard deviation) of the
837 components of the TOA energy budget breakdown. Mean values are bold where
838 they exceed the standard deviation. All fluxes in this table are considered posi-
839 tive downwards, such that a positive (negative) value means a net gain (loss) of
840 energy at the TOA due to each component. 42

841 **Table 2.** Pattern correlation between the TOA energy budget response to each individual
842 forcing and feedback term, calculated using the area-weighted Pearson-r cor-
843 relation coefficient. Note that (a) this only accounts for correlation between the
844 *pattern* of the TOA response to each surface property, and not the intensity, and
845 (b) the imposed albedo change is zero everywhere for a change in land surface
846 evaporative resistance. 43

Decrease in land albedo:											
	$dTOA_{net}$	$dSW_{TOA,net}$	$dLW_{TOA,net}$	dSW_{α_i}	dSW_{α_s}	dSW_q	dLW_q	dLW_{T_s}	dLW_T	dSW_{clouds}	dLW_{clouds}
mean	0.08	2.03	-1.95	1.60	0.52	0.42	2.03	-0.72	-2.77	-0.51	-0.49
std	0.65	0.38	0.39	0.04	0.10	0.05	0.26	0.06	0.55	0.37	0.21
Increase in land evaporative resistance											
	$dTOA_{net}$	dSW_{model}	dLW_{model}	dSW_{α_i}	dSW_{α_s}	dSW_q	dLW_q	dLW_{T_s}	dLW_T	dSW_{clouds}	dLW_{clouds}
mean	0.04	0.85	-0.81	0	0.15	0.18	0.97	-0.27	-0.8	0.52	-0.70
std	0.62	0.4	0.37	0	0.08	0.05	0.26	0.06	0.53	0.41	0.19

847 TABLE 1. Table of the globally averaged annual mean (and standard deviation) of the components of the TOA
848 energy budget breakdown. Mean values are bold where they exceed the standard deviation. All fluxes in this
849 table are considered positive downwards, such that a positive (negative) value means a net gain (loss) of energy
850 at the TOA due to each component.

TOA Breakdown Term	Pattern Correlation
Albedo (Snow/Ice)	0.38
SW Water Vapour	0.87
LW Water Vapour	0.89
LW from Surface Temperature	0.73
LW from Column Air Temperature	0.87
SW Cloud Effects	0.37
LW Cloud Effect	0.52
Total TOA <i>SW</i> Response	0.48
Total TOA <i>LW</i> Response	0.52
Total TOA net Response	0.33

851 TABLE 2. Pattern correlation between the TOA energy budget response to each individual forcing and feed-
852 back term, calculated using the area-weighted Pearson-r correlation coefficient. Note that (a) this only accounts
853 for correlation between the *pattern* of the TOA response to each surface property, and not the intensity, and (b)
854 the imposed albedo change is zero everywhere for a change in land surface evaporative resistance.

855 **LIST OF FIGURES**

856 **Fig. 1.** Total change in net TOA $SW + LW$ as a result of decreasing land albedo (left column) and
857 increasing land evaporative resistance (right column) for (a) the annual mean, (b) June-July-
858 August, and (c) December-January-February. The global mean value [W/m^2] of the change
859 in net TOA radiation is noted to the lower left of each panel. Only values that differ with
860 $p < 0.05$ in a students' t-test are shown. 46

861 **Fig. 2.** Map (and zonal average) of the change in annual mean precipitation for (a) a 0.1 decrease in
862 land surface albedo and (b) a 100 s/m increase in land surface evaporative resistance. Only
863 values with $p < 0.05$ in a student's t-test are shown for the maps. 47

864 **Fig. 3.** Change in annual mean net top of atmosphere energy fluxes [W/m^2] as a result of decreasing
865 land surface albedo. All fluxes (SW and LW) are shown positive down such that red colours
866 indicate more energy absorbed by the Earth system, while blue colours indicate more energy
867 lost by the Earth system. (a) shows the change in TOA net SW radiation from the imposed
868 change in albedo. (b) shows change in TOA net SW radiation from albedo changes to do
869 changes in snow and ice. (c) and (d) show, respectively, changes in TOA SW and LW radi-
870 ation from changes in column water vapour. (e) shows change in TOA LW from combined
871 changes in the surface radiative temperature and changes in air temperature. (f) shows the
872 total change in TOA $SW + LW$ from changes in cloud cover. The effect of cloud cover is
873 separated into its impact on TOA SW in (g) and TOA LW in (h). The area-weighted global
874 mean value for each term is shown to the lower left of each map. Only values that differ
875 with $p < 0.05$ in a students' t-test are shown. 48

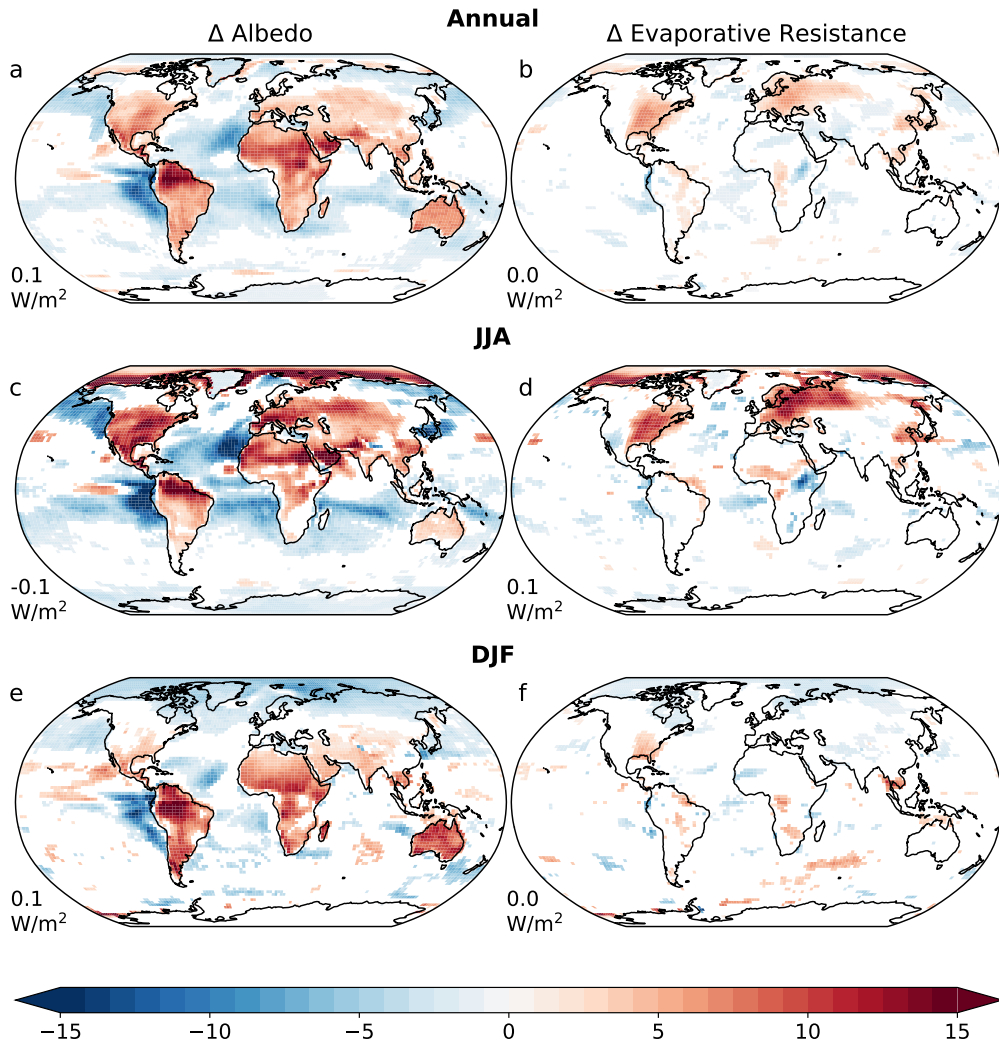
876 **Fig. 4.** Same as figure 3, but for an increase in land surface evaporative resistance. Note that in this
877 case, there is no imposed change in land surface albedo. 49

878 **Fig. 5.** Relationship between the zonal-mean latitude of the ITCZ (measured as the center of mass
879 of tropical precipitation ϕ_p) and the magnitude of cross-equatorial energy flux (in PW).
880 The relationship is shown for (a) the annual mean, (b) December/January/February, and
881 (c) June/July/August. Each small dot represents the annual average of a single year from
882 5 30-year model runs: a "baseline" simulation with a global land albedo of $\alpha = 0.2$ and
883 evaporative resistance of $r_s = 100s/m$, a dark land simulation with $\alpha = 0.1$, a bright land
884 simulation with $\alpha = 0.3$, a high evaporative resistance run with $r_s = 200$ s/m, and a low
885 evaporative resistance run with $r_s = 30$ s/m. The large grey circle shows the multi-year
886 average of the baseline ($\alpha = 0.2$, $r_s = 100s/m$) simulation, while the black square and red
887 triangle show the multi-year average of the dark ($\alpha = 0.1$) and high evaporative resistance
888 ($r_s = 200$ s/m) simulations, respectively. The slope of the linear relationship between cross-
889 equatorial atmospheric energy transport calculated using the TOA energy imbalance and
890 the ITCZ location is noted in the upper right of each panel, while the same relationship
891 calculated using vertically integrated moist static energy and meridional winds is noted in
892 brackets. 50

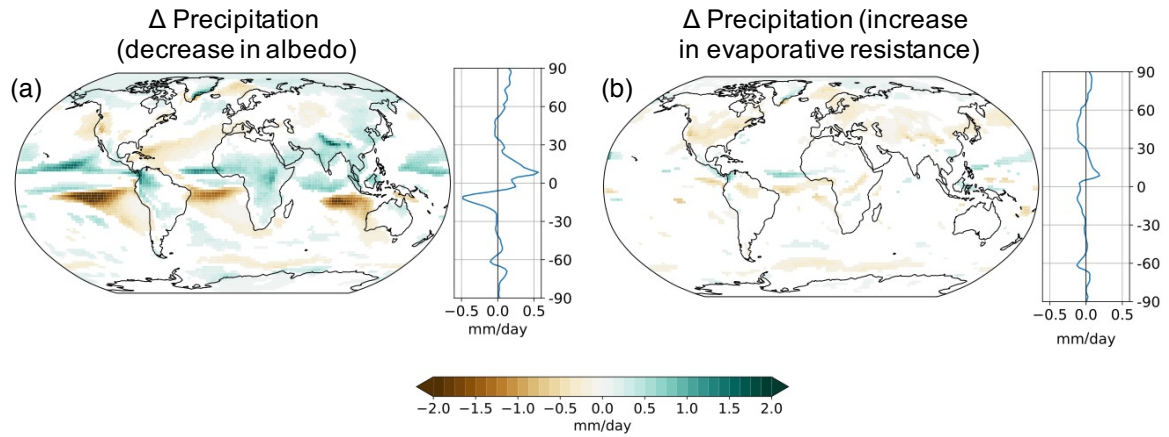
893 **Fig. 6.** The breakdown of the change in the zonally averaged annual mean location the ITCZ (mea-
894 sured by ϕ_p) resulting from each component, re-scaled to a 1° total northwards shift. Solid
895 (hatched) bars show the change in the zonal mean ITCZ location for a uniform decrease
896 of land surface albedo (increase of evaporative resistance). From left to right, bars show:
897 the total modelled change (dark grey); the change due to the sum of all of the individual
898 components (light grey); the change attributable to the imposed change in albedo (orange),
899 the change in albedo due to changes in snow and ice (yellow), LW effects due to changes
900 in surface temperature (dark purple), LW effects due to vertical changes in the atmospheric
901 temperature profile (lilac), SW changes due to changes in water vapour (light green), LW

902 changes due to changes in water vapour (dark green), *SW* changes due to changes in cloud
903 cover (light blue), and *LW* changes due to changes in cloud cover (dark blue). The magni-
904 tude of the ITCZ shift is noted above each bar, as well as the p value taken from a students'
905 t-test, where $p < 0.05$ indicates a significant shift from the baseline simulation. 51

Net TOA SW + LW

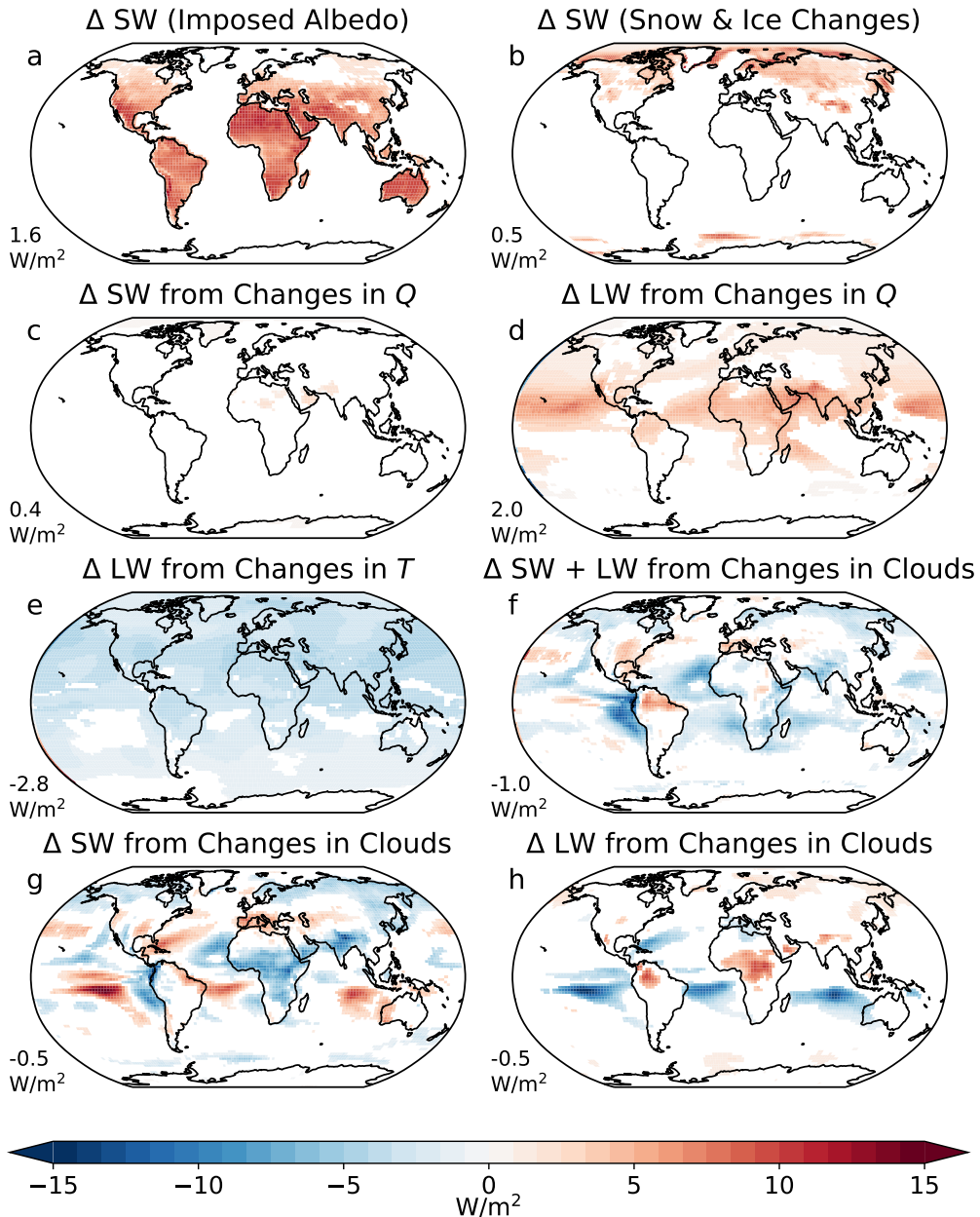


906 FIG. 1. Total change in net TOA $SW + LW$ as a result of decreasing land albedo (left column) and increasing
907 land evaporative resistance (right column) for (a) the annual mean, (b) June-July-August, and (c) December-
908 January-February. The global mean value [W/m^2] of the change in net TOA radiation is noted to the lower left
909 of each panel. Only values that differ with $p < 0.05$ in a student's t-test are shown.



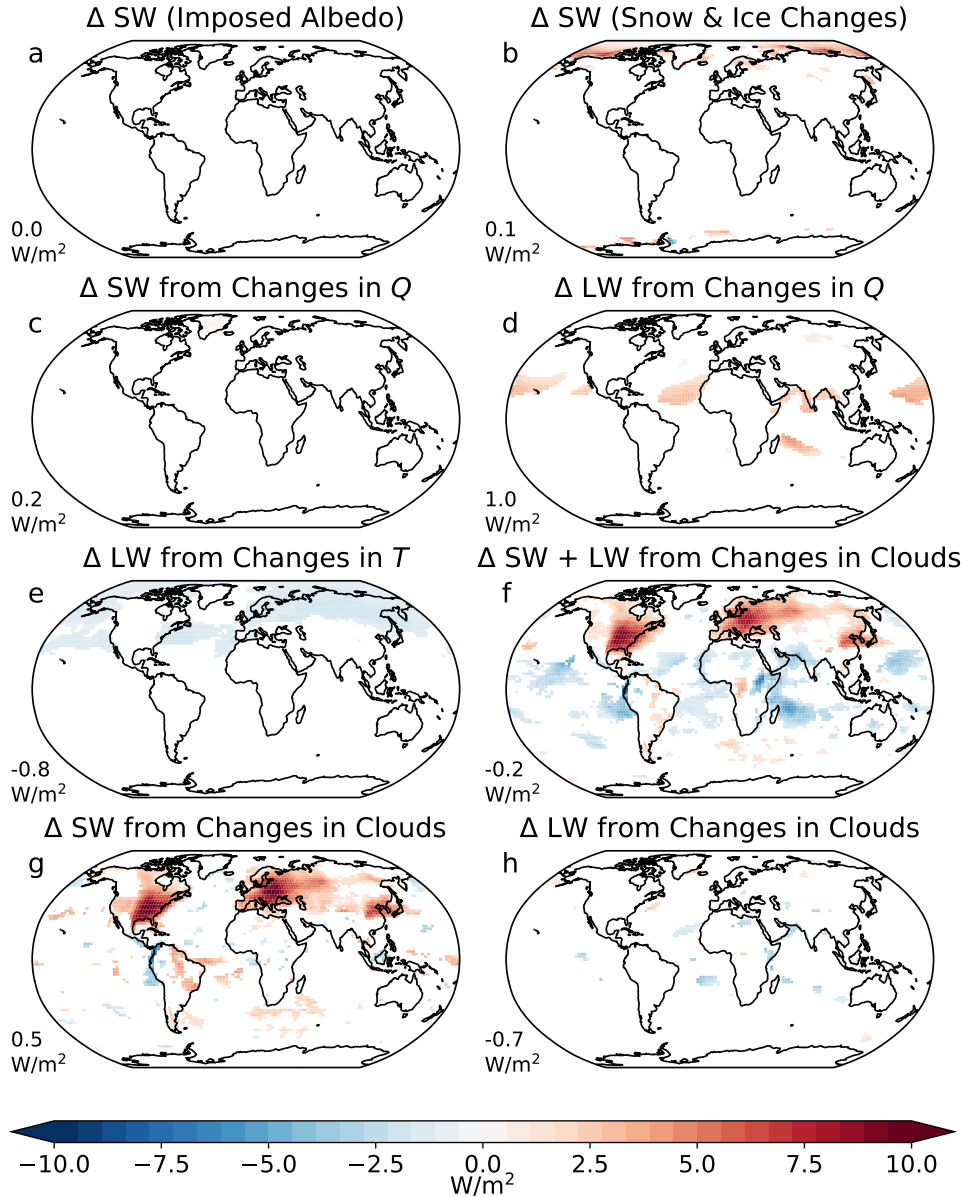
910 FIG. 2. Map (and zonal average) of the change in annual mean precipitation for (a) a 0.1 decrease in land
 911 surface albedo and (b) a 100 s/m increase in land surface evaporative resistance. Only values with $p < 0.05$ in a
 912 student's t-test are shown for the maps.

Net TOA flux breakdown, decrease in land albedo ANN



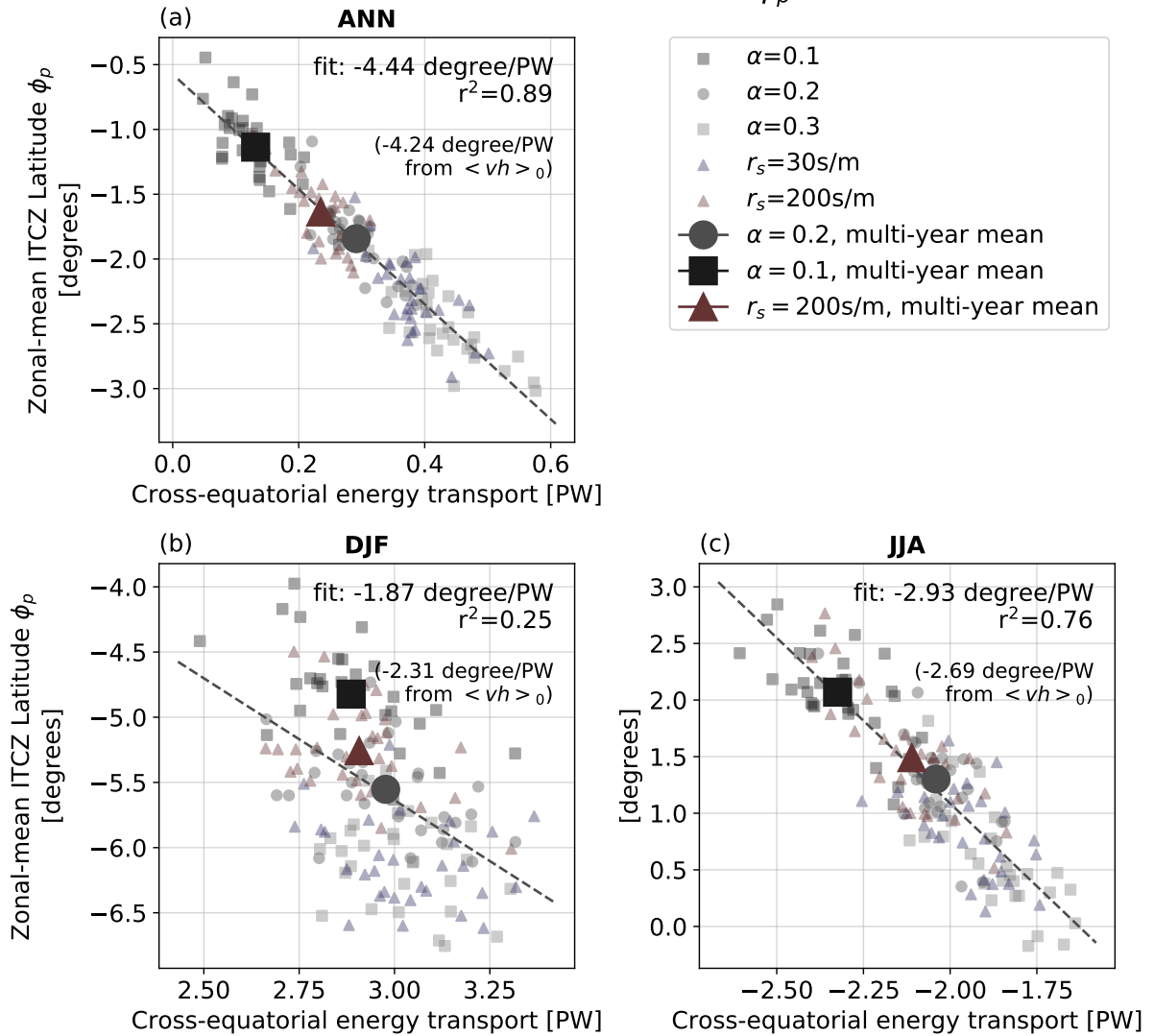
913 FIG. 3. Change in annual mean net top of atmosphere energy fluxes [W/m^2] as a result of decreasing land
 914 surface albedo. All fluxes (SW and LW) are shown positive down such that red colours indicate more energy
 915 absorbed by the Earth system, while blue colours indicate more energy lost by the Earth system. (a) shows the
 916 change in TOA net SW radiation from the imposed change in albedo. (b) shows change in TOA net SW radiation
 917 from albedo changes to do changes in snow and ice. (c) and (d) show, respectively, changes in TOA SW and LW
 918 radiation from changes in column water vapour. (e) shows change in TOA LW from combined changes in the
 919 surface radiative temperature and changes in air temperature. (f) shows the total change in TOA SW + LW from
 920 changes in cloud cover. The effect of cloud cover is separated into its impact on TOA SW in (g) and TOA LW
 921 in (h). The area-weighted global mean value for each term is shown to the lower left of each map. Only values

Net TOA flux breakdown, increase in land evaporative resistance (ANN)



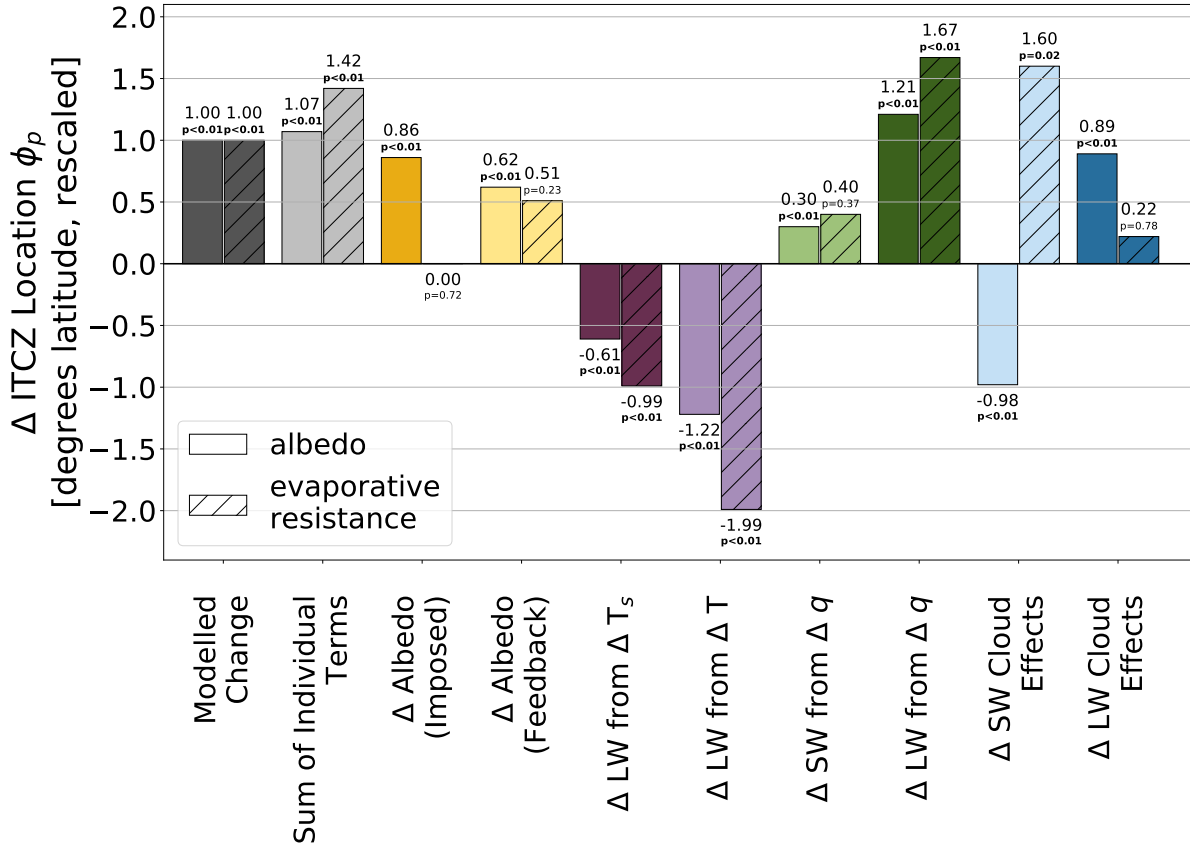
923 FIG. 4. Same as figure ??, but for an increase in land surface evaporative resistance. Note that in this case,
 924 there is no imposed change in land surface albedo.

Cross-equatorial Atmospheric Energy Transport vs. ITCZ Latitude ϕ_p



925 FIG. 5. Relationship between the zonal-mean latitude of the ITCZ (measured as the center of mass of tropical
 926 precipitation ϕ_p) and the magnitude of cross-equatorial energy flux (in PW). The relationship is shown for (a) the
 927 annual mean, (b) December/January/February, and (c) June/July/August. Each small dot represents the annual
 928 average of a single year from 5 30-year model runs: a “baseline” simulation with a global land albedo of $\alpha = 0.2$
 929 and evaporative resistance of $r_s = 100\text{s/m}$, a dark land simulation with $\alpha = 0.1$, a bright land simulation with
 930 $\alpha = 0.3$, a high evaporative resistance run with $r_s = 200$ s/m, and a low evaporative resistance run with $r_s = 30$
 931 s/m. The large grey circle shows the multi-year average of the baseline ($\alpha = 0.2$, $r_s = 100\text{s/m}$) simulation,
 932 while the black square and red triangle show the multi-year average of the dark ($\alpha = 0.1$) and high evaporative
 933 resistance ($r_s = 200$ s/m) simulations, respectively. The slope of the linear relationship between cross-equatorial
 934 atmospheric energy transport calculated using the TOA energy imbalance and the ITCZ location is noted in the
 935 upper right of each panel, while the same relationship calculated using vertically integrated moist static energy
 936 and meridional winds is noted in brackets.

Attribution of Δ ITCZ Location ϕ_p from Each TOA Breakdown Component (ANN)



937 FIG. 6. The breakdown of the change in the zonally averaged annual mean location the ITCZ (measured
 938 by ϕ_p) resulting from each component, re-scaled to a 1° total northwards shift. Solid (hatched) bars show the
 939 change in the zonal mean ITCZ location for a uniform decrease of land surface albedo (increase of evaporative
 940 resistance). From left to right, bars show: the total modelled change (dark grey); the change due to the sum of
 941 all of the individual components (light gray); the change attributable to the imposed change in albedo (orange),
 942 the change in albedo due to changes in snow and ice (yellow), LW effects due to changes in surface temperature
 943 (dark purple), LW effects to due vertical changes in the atmospheric temperature profile (lilac), SW changes due
 944 to changes in water vapour (light green), LW changes due to changes in water vapour (dark green), SW changes
 945 due to changes in cloud cover (light blue), and LW changes due to changes in cloud cover (dark blue). The
 946 magnitude of the ITCZ shift is noted above each bar, as well as the p value taken from a student's t-test, where
 947 $p < 0.05$ indicates a significant shift from the baseline simulation.